JETP Letters, Vol. 72, No. 9, 2000, pp. 445–448. Translated from Pis'ma v Zhurnal Éksperimental'noĭ i Teoreticheskoĭ Fiziki, Vol. 72, No. 9, 2000, pp. 641–646.

High Refractive Index and Other Optical Properties of Heterogeneous Media

A. N. Oraevskiĭ[1] and I. E. Protsenko[1,2,3]

[1] *Lebedev Institute of Physics, Russian Academy of Sciences, Leninskiĭ pr. 53, Moscow, 117924 Russia*

[2] *Applied Research Scientific Center, Joint Institute for Nuclear Research, Dubna, Moscow region, 141980 Russia*

[3] *e-mail: protsenk@stk.mmtel.ru*

Received August 17, 2000; in final form, September 29, 2000

Anomalously high values of the resonant refractive index, Rayleigh scattering extinction coefficient, and absorption or amplification are predicted for a heterogeneous medium composed of metallic nanoballs suspended in a transparent matrix. Optical characteristics of original materials do not posses resonant features.

PACS numbers: 78.20.Ci; 42.65.An; 42.70.-a

Optical materials with a high controlled refractive index n may have a variety of uses, e.g., for increasing the resolution of optical microscopes [1], controlling the direction of light beam propagation, and fabricating miniature high-quality lenses and other optical elements. There has been much discussion on the possibility of increasing n in a resonant medium with the help of the electromagnetically induced transparency (EIT) effect in conjunction with the Lorentz local field (LF) effect [2–7]. Therefore, the fabrication of a medium with large n is important both from the practical point of view and for studying fundamental effects such as the LF effect.

In this work, the optical properties of a nonresonant heterogeneous medium composed of small metallic clusters (nanoballs) in a transparent matrix are considered. The materials from which the nanoballs are made do not possess resonant optical features.

The dielectric constant of nanoballs in a matrix satisfies the Clausius–Mossotti relation [8, 9]

$$\frac{\varepsilon_{\text{mix}}(\lambda)-1}{\varepsilon_{\text{mix}}(\lambda)+2} = \frac{4\pi}{3}\sum_j \alpha_j(\lambda)N_j, \qquad (1)$$

where $\alpha_j(\lambda)$ is the polarizability of the particles of sort j and N_j is their concentration in the mixture. Below, we will analyze a heterogeneous medium composed of nanoballs suspended in a matrix and having radii no larger than several nanometers.

We assume that the nanoball radius r_b is much smaller than the wavelength. The nanoball polarizability $\alpha_b(\lambda)$ is given by the formula [10]

$$\alpha_b(\lambda) = r_b^3\frac{\varepsilon_b(\lambda)-1}{\varepsilon_b(\lambda)+2}, \qquad (2)$$

where $\varepsilon_b(\lambda) = \varepsilon_b'(\lambda) + i\varepsilon_b''(\lambda)$ is the complex dielectric constant of the material from which the nanoballs are made. In this case,

$$\frac{4\pi}{3}\alpha_b(\lambda)N_b = \eta\frac{\varepsilon_b(\lambda)-1}{\varepsilon_b(\lambda)+2}, \quad \eta = \frac{4\pi}{3}r_b^3N_b, \qquad (3)$$

where N_b is the nanoball concentration. Since the matrix volume comprises a $(1-\eta)$ fraction of the total volume, the dielectric constant of the system considered, according to Eq. (1), is determined by the relation

$$\frac{\varepsilon_{\text{mix}}(\lambda)-1}{\varepsilon_{\text{mix}}(\lambda)+2} = \eta\frac{\varepsilon_b(\lambda)-1}{\varepsilon_b(\lambda)+2} + (1-\eta)\frac{\varepsilon_m(\lambda)-1}{\varepsilon_m(\lambda)+2} \equiv \eta F_b(\lambda) + (\eta-1)F_m(\lambda). \qquad (4)$$

Let us analyze Eq. (4) for the particular case of silver nanoballs suspended in a transparent optical glass. The $\varepsilon_b(\lambda) \equiv \varepsilon_b'(\lambda) + i\varepsilon_b''(\lambda)$ and $\varepsilon_m(\lambda) \equiv \varepsilon_m'(\lambda)$ functions were taken from [11, 12] (Fig. 1). The $\varepsilon_{\text{mix}}(\lambda)$ functions calculated by Eq. (4) for different η values are shown in Fig. 2. As distinct from the monotonic change in the characteristics of initial materials with changing wavelength (Fig. 1), the curves in Fig. 2 exhibit a pronounced resonance behavior, with $\varepsilon_{\text{mix}}'(\lambda)$ and $\varepsilon_{\text{mix}}''(\lambda)$ sharply increasing at resonances and in their vicinity.

The refractive index $n_{\text{mix}}(\lambda) \equiv \text{Re}[\varepsilon_{\text{mix}}(\lambda)]^{1/2}$ and the absorption coefficient $\kappa_{\text{mix}}(\lambda) \equiv \text{Im}[\varepsilon_{\text{mix}}(\lambda)]^{1/2}$ of the heterogeneous system are shown in Fig. 3 for different η values. For $\eta = 0.4$, the maximum value $\max(n_{\text{mix}}) \approx 10$. To the right of maximal n, where the absorption is relatively weak, $n_{\text{mix}}(\lambda) \sim 4$–$6$ is rather large. The wavelength λ_r corresponding to the resonance can be deter-

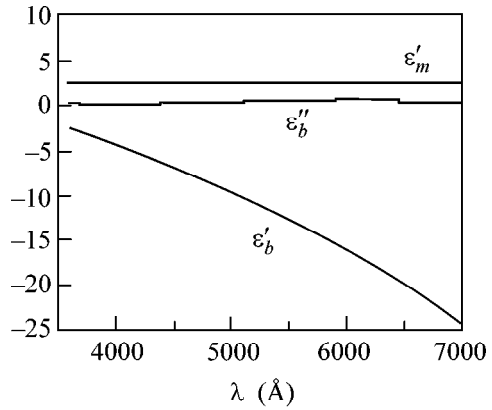

Fig. 1. Dielectric constants of silver and optical glass.

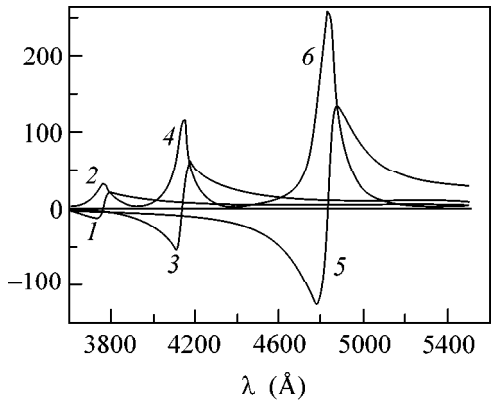

Fig. 2. The functions (*1*, *3*, *5*) $\varepsilon'_{\text{mix}}(\lambda)$ and (*2*, *4*, *6*) $\varepsilon''_{\text{mix}}(\lambda)$ for η = (*1*, *2*) 0.2, (*3*, *4*) 0.4, and (*5*, *6*) 0.6.

mined from the relationship $\varepsilon'_{\text{mix}}(\lambda_r) = 0$, which can be shown to be equivalent to

$$\eta = \eta_r(\lambda) \equiv 0.5[-P(\lambda) + \sqrt{P^2(\lambda) + Q(\lambda)}], \qquad (5)$$

where

$$P(\lambda) = [\mathrm{Re}F_b(\lambda) - F_m(\lambda)]$$
$$\times [2F_m(\lambda) - 0.5]/\{[\mathrm{Re}F_b(\lambda) - F_m(\lambda)]^2 + [\mathrm{Re}F_b(\lambda)]^2\},$$
$$Q(\lambda) = 2[2F_m(\lambda) + 1]$$
$$\times [1 - F_m(\lambda)]/\{[\mathrm{Re}F_b(\lambda) - F_m(\lambda)]^2 + [\mathrm{Im}F_b(\lambda)]^2\}.$$

The λ_r value for a given η can be found from the graph $\eta = \eta_r(\lambda_r)$ (Fig. 4).

Let us determine the Rayleigh scattering extinction coefficient $h(\lambda)$ for the heterogeneous medium. According to Eq. (120.1) in [10],

$$h(\lambda) = \frac{(2\pi)^2}{3\lambda^3} V \langle \delta\varepsilon_{\text{mix}}(\lambda)\delta\varepsilon^*_{\text{mix}}(\lambda)\rangle. \qquad (6)$$

Here, $\delta\varepsilon_{\text{mix}}(\lambda)$ is the dielectric constant fluctuation in the volume V of the heterogeneous medium and $\langle\ldots\rangle$ stands for the statistical averaging. The $\delta\varepsilon_{\text{mix}}(\lambda)$ value can be evaluated using relationships (4), yielding

$$\delta\varepsilon_{\text{mix}}(\lambda) = \frac{[\varepsilon_{\text{mix}}(\lambda) + 2]^2}{\varepsilon_m(\lambda) + 2}$$
$$\times \left[\delta\eta \frac{\varepsilon_b(\lambda) - \varepsilon_m(\lambda)}{\varepsilon_b(\lambda) + 2} + \frac{\varepsilon_m(\lambda) + 2}{3}\frac{\delta N_m}{N_m}\right], \qquad (7)$$

where N_m is the atom concentration in the matrix material and δN_m is its fluctuation in the volume V. The averaging is carried out under the assumption that the fluctuations $\delta\eta$ and δN_m are statistically independent. For the Poisson fluctuations of the total number $N_{mV} = VN_m$ of the matrix atoms in V, one has $\langle \delta N^2_{mV}\rangle = N_{mV}$ and $\langle \delta N^2_m\rangle = N_m/V$. Taking into account that $\delta\eta \equiv \eta(V_b N_b)$, where V_b is the average volume of a nanoball, one can obtain $\delta\eta = (V_b/V)\delta N_{bV} + (1/V)\delta V_{bV}$, where $N_{bV} \equiv N_b V$ is the total number of nanoballs and $V_{bV} \equiv N_{bV}V_b$ is the total volume they occupy in V. Assuming that the fluctuations of N_{bV} and V_{bV} are also of the Poisson type, one gets $\langle \delta N^2_{bV}\rangle = N_{bV}$ and $\langle \delta V^2_{bV}\rangle = N_{bV}\langle \delta V^2_b\rangle$. Let us write for the fluctuations δV_b of the nanoball volume $\langle \delta V^2_b\rangle \equiv (p-1)V^2_b = (p-1)\eta^2/N^2_b$, where $p \geq 1$ is a dimensionless parameter. Substituting $\delta\varepsilon_{\text{mix}}(\lambda)$ from Eq. (7) in Eq. (6) and taking the average, one obtains

$$h(\lambda) = \frac{(2\pi)^2}{3\lambda^3}\frac{|\varepsilon_{\text{mix}}(\lambda) + 2|^4}{[\varepsilon_m(\lambda) + 2]^2}$$
$$\times \left\{\frac{\eta^2 p}{N_b}\left|\frac{\varepsilon_b(\lambda) - \varepsilon_m(\lambda)}{\varepsilon_b(\lambda) + 2}\right|^2 + \frac{(1-\eta)^2}{9N_m}[\varepsilon_m(\lambda) - 1]^2\right\}. \qquad (8)$$

The functions $h(\lambda)$ are shown in Fig. 3 (curves *3*, *6*) for $N_b = 10^{20}$ cm^{-3} and $p = 1.1$. One can see that for $\eta = 0.2$ the Rayleigh scattering is weaker than the absorption, but for $\eta = 0.4$ its maximum is appreciably higher than the absorption maximum and the $h(\lambda)$ curve has a pronounced resonance. The Rayleigh scattering also increases with an increase in the nanoball radius.

The absorption in the heterogeneous medium can be suppressed if an active matrix is used. Let the active matrix amplify due to the excited impurity atoms, whose concentration is much smaller than the concentration of the main atoms of the matrix. We also assume that the impurity atoms amplify resonantly at a wavelength λ_0 and that the amplification and dispersion curves are Lorentzian. The dielectric constant of the main matrix atoms is assumed to be the same as shown

in Fig. 1. For such heterogeneous systems one has, according to the Clausius–Mossotti formula,

$$\frac{\varepsilon_{mix}(\lambda)-1}{\varepsilon_{mix}(\lambda)+2} = \eta\frac{\varepsilon_b(\lambda)-1}{\varepsilon_b(\lambda)+2} + (1-\eta)\left[\frac{\varepsilon_m(\lambda)-1}{\varepsilon_m(\lambda)+2}+\frac{G}{\delta(\lambda)/\gamma+i}\right]\equiv F(\lambda). \quad (9)$$

In Eq. (9), $\delta(\lambda) = 2\pi c(\lambda^{-1} - \lambda_0^{-1})$ is the detuning from the amplification resonance, c is the velocity of light in free space, γ is the linewidth of active transition, and G is the amplification parameter.

Let us determine the conditions under which the active heterogeneous medium does not absorb while $n_{mix} \gg 1$. Resolving Eq. (9) for $\varepsilon_{mix}(\lambda)$, one obtains

$$\varepsilon_{mix}(\lambda) = \frac{1+2F(\lambda)}{1-F(\lambda)}. \quad (10)$$

It follows from Eq. (10) that $\varepsilon_{mix}(\lambda)$ is real if $\mathrm{Im}[F(\lambda)] = 0$. For $\lambda = \lambda_0$, this condition gives $G = G_{tr}$, where

$$G_{tr} = \frac{\eta}{1-\eta}\mathrm{Im}\left[\frac{\varepsilon_b(\lambda_0)-1}{\varepsilon_b(\lambda_0)+2}\right]. \quad (11)$$

Let $G = G_{tr}$; then $\varepsilon_{mix}(\lambda_0) \gg 1$ if $F(\lambda_0) \equiv \mathrm{Re}[F(\lambda_0)] \longrightarrow 1$, which holds for

$$\eta \longrightarrow \eta_\infty \equiv \frac{3}{(\varepsilon_m(\lambda_0)+2)\mathrm{Re}[(\varepsilon_b(\lambda_0)-1)/(\varepsilon_b(\lambda_0)+2)]}, \quad \eta < \eta_\infty. \quad (12)$$

The necessary condition $0 < \eta_\infty < 1$ is fulfilled if $\mathrm{Re}[(\varepsilon_b(\lambda_0)-1)/(\varepsilon_b(\lambda_0)+2] > 1$. This is true for all $\varepsilon_b(\lambda)$ values in the curve in Fig. 1. Therefore, one can create a virtually transparent heterogeneous medium with a high refractive index at a certain wavelength if $G \approx G_{tr}$ and $\eta \approx \eta_\infty$. The $n_{mix}(\lambda)$ and $\kappa_{mix}(\lambda)$ functions are shown in Fig. 5 for $G = 1.01G_{tr}$, $G_{tr} = 0.135$, $\lambda_0 = 3750$ Å, $\gamma = 10^{13}$ s^{-1}, $\eta = 0.98\eta_\infty$, and $\eta_\infty = 0.193$. Under these conditions, one can ignore the Rayleigh scattering, because it is small even at $\eta = 0.2$ (curve *3* in Fig. 3). At $\lambda = \lambda_0$, the heterogeneous medium is absolutely transparent and its refractive index is $n_{mix} = 10.6$ at $\eta = 0.96\eta_\infty$ and $n_{mix} = 15$ at $\eta = 0.98\eta_\infty$. The amplification occurs in a certain vicinity of $\lambda = \lambda_0$. For $G_{tr} = 0.135$, the amplification in the matrix material should be e-fold at a length of $\approx$0.2 μm. This is several times higher than the practically achievable amplification length in semiconductor lasers. However, it is hoped that the G_{tr} value may be reduced by the special choice of the nanoball material.

At $G > G_{tr}$, $\varepsilon''_{mix} < 0$ in a small vicinity of λ_0 and is much greater in magnitude than for the matrix without nanoballs (Fig. 6), indicating a giant amplification. For example, the maximal $\varepsilon''_{mix} = -989.2$ (Fig. 6), whereas in the matrix with the same parameters but without nanoballs, $\varepsilon''_{mix} \approx -17$.

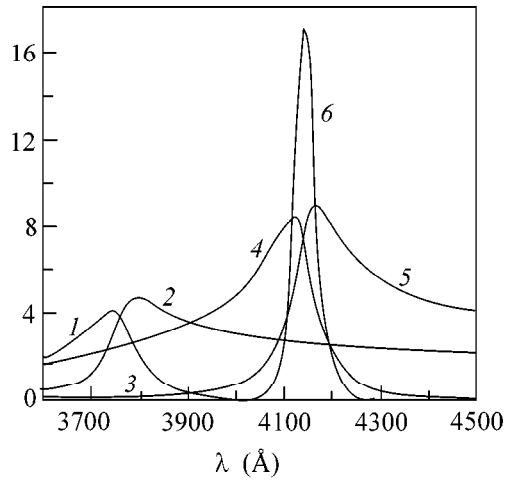

Fig. 3. (*2*, *5*) Refractive index $n_{mix}(\lambda)$, (*1*, *4*) amplification coefficient $\kappa_{mix}(\lambda)$, and (*3*, *6*) Rayleigh scattering extinction coefficient $h(\lambda)$ for η = (*1*, *2*, *3*) 0.2 and (*4*, *5*, *6*) 0.4.

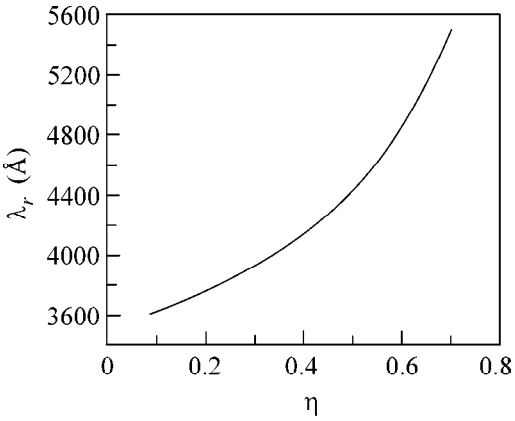

Fig. 4. The λ_r wavelength corresponding to the resonance in a heterogeneous medium composed of silver nanoballs suspended in an optical glass, as a function of the nanoball volume concentration.

At the λ_{cr} point defined by equation $\varepsilon''_{mix} = 0$, the refractive index is zero if $\varepsilon'_{mix} < 0$. The interval of wavelengths in the vicinity of λ_{cr} is thus of interest for electrodynamics and calls for special investigation.

Two main causes are at the origin of the optical properties of heterogeneous media described above. First, the Clausius–Mossotti formula takes into account that the local field acting on a particle differs from its mean value. The second cause is that the metallic nanoballs are taken as a component of a heterogeneous medium. For metals, $\varepsilon'_b < 0$ in the optical range, and

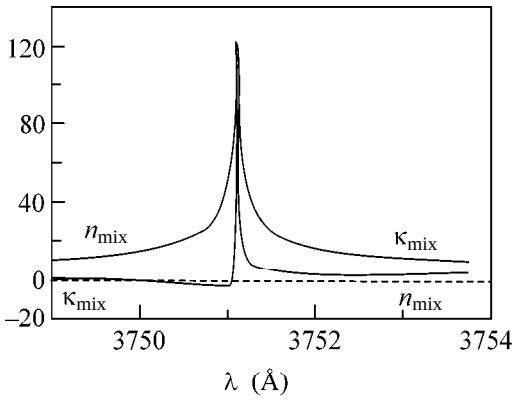

Fig. 5. Refractive index $n_{mix}(\lambda)$ and absorption coefficient $\kappa_{mix}(\lambda)$ of an active heterogeneous medium with $\eta = 0.98\eta_\infty$ and $G = G_{tr}$.

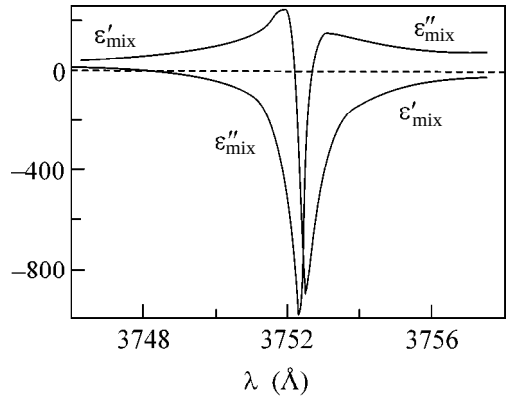

Fig. 6. The functions $\varepsilon'_{mix}(\lambda)$ and $\varepsilon''_{mix}(\lambda)$ in the vicinity of the amplification maximum for $\eta = 0.96\eta_\infty$ and $G = 1.1G_{tr}$.

this underlies the resonant behavior of the dielectric constant of a heterogeneous medium. Note, in this connection, that the metallic microspheres strongly influence the spontaneous emission rate for a nearby dipole [13–15]. Heterogeneous media with the properties considered in this work can also be created using different (including resonant) media for which $\mathrm{Re}[\varepsilon_b(\lambda)] < 0$. It follows from Eq. (4) that a material with $\varepsilon'_b(\lambda) \approx -2$ and $\varepsilon''_b(\lambda) \ll 1$ is most appropriate for the nanoballs.

Experimental studies of the optical properties of heterogeneous media are of interest both for revealing possible practical applications of such media and for studying fundamental effects caused by the difference between the local field and its mean. Because of the strong absorption, film thicknesses for passive heterogeneous media should be $\leq\lambda$ or ε_{mix} should be determined from the reflected emission, e.g., using ellipsometry.

A heterogeneous medium with an active matrix can, in principle, have a very high amplification coefficient and thus can be used for the fabrication of subminiature laser elements.

This work was supported by the Russian Foundation for Basic Research (project no. 00-216660) and the Applied Research Scientific Center, Joint Institute for Nuclear Research, Dubna. We are grateful to V.S. Zuev. I.E. Protsenko thanks O.A. Zaĭmidoroga and V.N. Samoĭlov (ARSC, Dubna) for helpful consultations and interest in the work.

REFERENCES

1. B. Born and E. Wolf, *Principles of Optics* (Pergamon, Oxford, 1980).
2. M. O. Scully, Phys. Rev. Lett. **67**, 1855 (1991).
3. M. Fleischhauer, C. H. Keitel, and M. O. Scully, Phys. Rev. A **46**, 1468 (1992); M. O. Scully and M. Fleischhauer, Phys. Rev. Lett. **69**, 1360 (1992); M. O. Scully and Shi-Yao Zhu, Opt. Commun. **87**, 134 (1992); S. E. Harris, J. E. Field, and A. Kasapi, Phys. Rev. A **46**, R29 (1992).
4. A. S. Zibrov, M. D. Lukin, L. Hollberg, *et al.*, Phys. Rev. Lett. **76**, 3935 (1996).
5. J. P. Dowling and C. M. Bowden, Phys. Rev. Lett. **70**, 1421 (1993).
6. M. E. Crenshaw and C. M. Bowden, Phys. Rev. A **53**, 1139 (1996).
7. J. A. Leegwater and Saul Mukamel, Phys. Rev. A **49**, 146 (1994).
8. *Physics Encyclopedia* (Sov. Éntsiklopediya, Moscow, 1990), Vol. 2.
9. C. J. Bottcher, *Theory of Electric Polarization* (Elsevier, Amsterdam, 1973).
10. L. D. Landau and E. M. Lifshitz, *Course of Theoretical Physics*, Vol. 8: *Electrodynamics of Continuous Media* (Nauka, Moscow, 1982; Pergamon, New York, 1984).
11. G. T. Boyd, Th. Rasing, J. R. R. Leite, and Y. R. Shen, Phys. Rev. B **30**, 519 (1984).
12. *Handbook of Physical Data*, Ed. by I. S. Grigor'ev and E. Z. Melikhova (Nauka, Moscow, 1991), p. 767.
13. V. V. Klimov, Doctoral Dissertation in Mathematical Physics (Fiz. Inst. Ross. Akad. Nauk, Moscow, 1999).
14. S. Nie and S. R. Emory, Science **275**, 1102 (1997); H. F. Hamman, A. Gallagher, and D. J. Nesbitt, Appl. Phys. Lett. **76**, 1953 (2000).
15. M. B. Mohamed, V. Volkov, S. Link, and M. A. El-Sayed, Chem. Phys. Lett. **317**, 517 (2000).

Translated by V. Sakun

JETP Letters, Vol. 72, No. 9, 2000, pp. 449–452. Translated from Pis'ma v Zhurnal Éksperimental'noĭ i Teoreticheskoĭ Fiziki, Vol. 72, No. 9, 2000, pp. 647–652.

Nonexponential Dynamics and Competition between Quasi-trapped States in an *N*-Atomic Micromaser

G. P. Miroshnichenko[1,2], I. P. Vadeĭko[1], A. V. Rybin[3], and J. Timonen[3]

[1] *Institute of Fine Mechanics and Optics, ul. Sablinskaya 14, St. Petersburg, 197101 Russia*

[2] *e-mail: mirosh@mkk.ifmo.ru*

[3] *Department of Physics, University of Jyväskylä, Jyväskylä, Finland*

Received September 4, 2000; in final form, October 27, 2000

Transient processes are examined for the reduced density matrix (RDM) of the quantum mode of a micromaser pumped by clusters of *N* two-level atoms. The RDM dynamics consists of the fast and slow stages. The hierarchy of time scales is explained by the fact that the spectrum of the operator of RDM evolution contains groups of eigenvalues concentrated near zero and unity. A convenient basis for describing the fast stage is provided by a set of eigenvectors and adjoint vectors of Jordan cells related to the degenerate zero eigenvalue. The dynamics of the adjoint vector as a function of the number of passed clusters is nonexponential. One adjoint vector transforms jumpwise into the neighboring vector upon the passage of the next cluster. The slow stage of dynamics is controlled by the quasi-trapped states (QTSs) of the field. These states are the generalization of the trapped states of the ideal one-atom model and can be represented as linear combinations of the long-lived eigenvectors of the evolution operator with eigenvalues close to unity. An important feature of the QTSs is their stability to fluctuations of the number of atoms in clusters and to the field relaxation rate. © *2000 MAIK "Nauka/Interperiodica"*.

PACS numbers: 42.50.Md

Considerable technological progress in resonator electrodynamics [1] made it possible to design a new physical device—a micromaser on Rydberg atoms [2]. Most publications are focused on the standard one-atomic model [3–6], when a resonator contains no more than one atom at any time instant. The basic assumptions of the theory are the following. Due to the large kinetic energy E_{kin} of an atom, its center of mass moves along the classical trajectory; the field relaxation during the atom–field interaction is ignored because of the high *Q*-factor of the resonator; and the spontaneous atomic relaxation is ignored because the lifetime of the Rydberg states is large, as compared to the duration τ of atom–field interaction, and the coupling constant *g* is large because of the large dipole moment of these states. The field relaxation is taken into account at time instants when the resonator is empty. These assumptions can be formulated as

$$R\tau \ll 1, \quad \tau\gamma \ll 1, \quad g\tau \geq 1, \quad E_{\text{kin}} \gg \hbar\omega, \qquad (1)$$

where R [s^{-1}] is the atomic flux density with the Poisson distribution of the intervals between *N*-atomic clusters and $\gamma^{-1} = Q/\omega$ is the photon lifetime in the resonator. In addition, the field nonuniformity in the resonator is usually neglected.

We aim at studying the transient processes of field transition to a steady state in the *N*-atomic generalization introduced in [7] for an ideal one-atomic model. Periodic sequences of *N*-atomic clusters excited to the Rydberg levels by an auxiliary laser are passed through the resonator. If the cluster volume *V* is small compared to the wavelength λ of the normal mode of the resonator, i.e., $V \approx (0.01\lambda)^3$, the field may be considered constant in the cluster. For the standard frequency ω = 20 GHz of the mode [2] and a cluster of about 10 atoms, the necessary density of excited atoms should be 10^4 cm^{-3}. Simple estimations demonstrate that there are no principle difficulties in preparing excited atoms with such density. In particular, if the cross section for the absorption of ground-state atoms is $\sigma \sim 10^{-16}$ cm^2, the waist of an auxiliary laser is $\varpi \sim$ 30 μm [8], the excitation efficiency is about 1%, and the initial flux density is ~10^8 cm^{-3}, a laser with output of about 1 kW/cm^2 and pulse duration $\tau_{\text{ex}} = 0.01\lambda/v_{\text{at}} \sim$ 1 μs, where $v_{\text{at}} \approx 300$ m/s is the mean velocity of atoms in the flux, is needed.

The *N*-atomic model is described by the Hamiltonian [9]

$$H = H_0 + V = \omega\left(a^\dagger a + S_3 + \frac{N}{2}\right) + g(a^\dagger S_- + aS_+), \qquad (2)$$

where S_3 and $S_\pm$ are the generators of SU(2) algebra [10]; a and $a^\dagger$ are the operators of, respectively, creation and annihilation of the field mode of the resonator; and $\hbar = 1$. Let $\hat{W}(N, \tau)$ be the operator of evolution of the reduced density matrix (RDM). If, before a new cluster enters the resonator, the field is described by the density

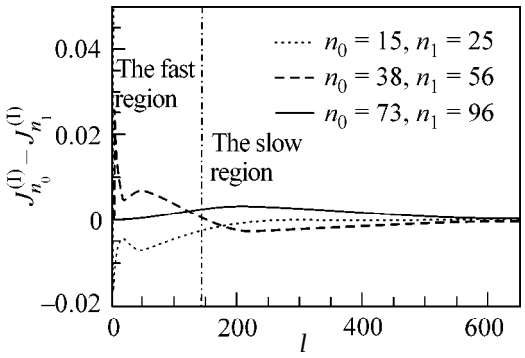

Fig. 1. The rate of changing the integral probability [see Eq. (6)] in three successive quasi-trapping regions for the initial coherent state of the field with the mean number of photons 16 and the number of atoms in cluster $N = 5$.

matrix $\rho_f(t)$, then, after the cluster has left the resonator, it takes the form

$$\begin{aligned}\rho_f(t+\tau) &= \mathcal{W}(N,\tau)\rho_f(\tau)\\ &= \mathrm{Tr}_{\mathrm{at}}\{e^{-iH\tau}\rho_{\mathrm{at}}\otimes\rho_f(t)e^{iH\tau}\}.\end{aligned} \tag{3}$$

The field relaxation is described by the standard Liouville operator $\mathcal{L}$ [3, 5]. Following Filipowicz's formalism [3] for periodical pumping of a micromaser by the Poissonian flux of atomic clusters, one can construct the entire superoperator of RDM evolution:

$$\begin{aligned}\mathcal{S}(N) &= \mathcal{Q}(N_{\mathrm{ex}})\mathcal{W}(N,\tau)\\ &= (1-\mathcal{L}/N_{\mathrm{ex}})^{-1}\mathcal{W}(N,\tau).\end{aligned} \tag{4}$$

In [11], it was shown that the dynamics of the RDM of a micromaser field has an important property of diagonal invariance: given some integral of motion, each RDM's diagonal evolves independently of the other matrix elements of the RDM. This considerably simplifies the calculations.

In this work, we analyze the photon statistics in a resonator through which the clusters of excited atoms are passed. In the presence of diagonal invariance, it is sufficient to examine the dynamics only of the central RDM's diagonal—the photon number distribution function. To do this, it is convenient to introduce a linear vector space in which the central diagonal is represented by the column vector $\rho_n^{(l)}$, while the evolution operator is represented by a matrix. In this space, a vector having only one nonzero element (equal to unity) and representing the density matrix of a pure Fock state is referred to as the Fock vector.

To describe the dynamics of photon number populations, the probability flux vector is introduced:

$$J_n^{(l)} = \sum_{n'=0}^{n-1}\sum_{n''=n}^{\infty}(-\mathcal{S}(N)_{n'n''}\rho_{n''}^{(l)} + \mathcal{S}(N)_{n''n'}\rho_{n'}^{(l)}), \tag{5}$$

where $\rho^{(l)}$ is the central diagonal of the matrix ρ_f after the passage of l clusters. The number l plays the role of discrete time in this problem. The vector $J^{(l)}$ has the meaning of the population fraction "passed" through the nth Fock state and allows one to estimate the rate of changing the integral probability in the interval $[n_0, n_1)$ after the passage of the lth cluster:

$$J_{n_0}^{(l)} - J_{n_1}^{(l)} = \sum_{n'=n_0}^{n_1-1}(\rho_{n'}^{(l)} - \rho_{n'}^{(l-1)}). \tag{6}$$

Numerical simulations demonstrated that the transient process of micromaser excitation by passing polyatomic clusters has fast and slow stages with respect to the discrete time l. After several first passes, the initial distribution extending over a wide range of Fock numbers is broken into narrow peaks localized in well-defined (referred to as quasi-trapping) regions of photon numbers. The population of the Fock states is rapidly transferred from the intermediate regions, referred to as zero zones, to the quasi-trapping regions. Then, the quasistationary regime is established, during which the dynamics consists of a slow population flow between different quasi-trapping regions toward the large Fock numbers.

The fast and slow stages are shown in the plot of the change per pass in the integral probability in the quasi-trapping regions vs. the number of passed clusters (Fig. 1). The character of the transient process is explained by the specific structure of evolution operator (3). The matrix $\mathcal{W}$ has the lower triangular form, and its spectrum coincides with the set of its diagonal elements. It is natural to number the eigenvalues and eigenvectors using the Fock number n in the order of their positioning on the diagonal of $\mathcal{W}$. The set of eigenvalues contains two important regions, close to unity and to zero. The points close to unity are in the quasi-trapping regions, and the zero zones are filled with the numbers close to zero. It is seen from Fig. 2 that, as the number of atoms in a cluster increases, the spectrum changes only slightly in the vicinity of unity but the number of zero points increases. Such behavior is explained by a decrease in the number of intermediate eigenvalues. For this reason, the spectrum for large N contains large zero regions and a comparatively small number of points close to unity. The fast stage of the transient process in the discrete time l is obviously related to the zero zones of the spectrum. Since the spectrum is close to degeneracy, it is natural to describe the dynamics in the zero-approximation basis, which is constructed by setting equal to zero all diagonal elements of $\mathcal{W}$ in the zero zones. An analysis shows that the resulting matrix $\mathcal{W}$ contains Jordan cells, while the basis set of eigenvectors of each zone is incomplete. This can be proved by contradiction: in the case of completeness, the basis elements can form linear combinations having a single component in the zero zone. However, these combinations are eigenvectors only if

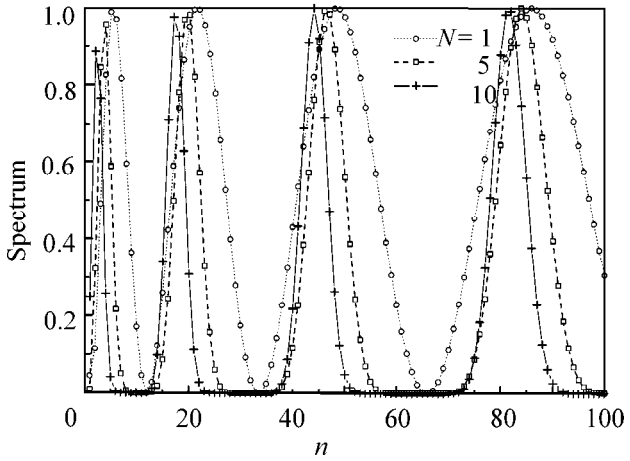

Fig. 2. The spectrum $\mathcal{W}(N)$ for $N = 1$, 5, and 10.

the matrix $\mathcal{W}$ entirely contains the zero block whose diagonal is occupied by the zero zone at hand. In our case, such blocks are absent, because the matrix $\mathcal{W}$ is random, has the bandlike lower triangular form, and the width of even the second zero zone exceeds the number of atoms.

In this study, we focused on some dynamical features that are associated with inclusion of the adjoint vectors into the basis set. The dynamics of an eigenvector is governed by a discrete exponential, i.e., by the exponential function λ^l, where λ is the eigenvalue of this vector. The dynamics of an adjoint vector is nonexponential, because the evolution operator transforms one adjoint vector into the other from the same Jordan cell. The presence of these vectors explains the rapid population transfer through the zero zones, with the rate being restricted by the number of atoms in the cluster. Otherwise, the dynamics described by the eigenvectors with zero eigenvalues would take the form of instantaneous population transfer through the zero zone, in contradiction to the above-mentioned restriction. Interestingly, the limiting pumping rate, equal to N photons per passage of an N-atomic cluster, is attained at the center of the zero zone.

The slow (quasistationary) stage of field evolution is related to the eigenvectors corresponding to the eigenvalues close to unity. In the one-atomic model of a micromaser, the so-called trapped states are known [12]. These are the undecaying states representable as Fock vectors for which the number n of the nonzero component satisfies the trapping condition

$$\sqrt{n+1} = \frac{\pi\chi}{g\tau}, \quad \chi = 0, 1, \ldots . \tag{7}$$

This condition also provides an estimate for the positions of the centers of quasi-trapping regions in the polyatomic model (see Fig. 2). By analogy with the one-atomic case, we introduce the notion of the quasi-trapped state (QTS) as a linear, localized (in the Fock basis) combination of eigenvectors corresponding to the eigenvalues close or equal to unity. It is precisely the localization regions that are the quasi-trapping regions.

It should be noted that the concept of a micromaser pumped by N-atomic clusters was discussed earlier [7], where attention was focused on the stationary state. The authors of [13] pointed out that various fluctuations in the system and field relaxation destroy the exact trapped states that were found in the ideal one-atomic model. In this study, we emphasize that the operator of RDM evolution has two specific features concerning QTSs. The first one is that the eigenvalues close to unity and the corresponding eigenvectors are much more stable to relaxation for larger numbers of atoms in the cluster and, therefore, the quasistationary stage has the form of a macroscopic QTS superposition with an essentially sub-Poissonian width of each peak and is stable to external losses. The second feature is a weak dependence of the positions of QTS centers on the number N of atoms in the cluster (see Fig. 2). This leads us to the important conclusion that the form of the field quasistationary state is stable to the fluctuations of the number of atoms in the cluster. This result is corroborated by the graphs in Fig. 3, where the quasistationary distribution obtained by taking into account the scatter of the number of atoms in the cluster (Fig. 3a) is compared with the same for a fixed number of atoms in the cluster (Fig. 3b). The calculations were carried out using the Gaussian distribution function with mean number of atoms 15 and standard deviation 3. The presence of scatter results in shortening of the QTS lifetime, which is manifested as a speedup of the transition from one quasistationary state to the next one. In the graphs, this is reflected by the fact that the numbers l of iterations required for attaining the given distribution are

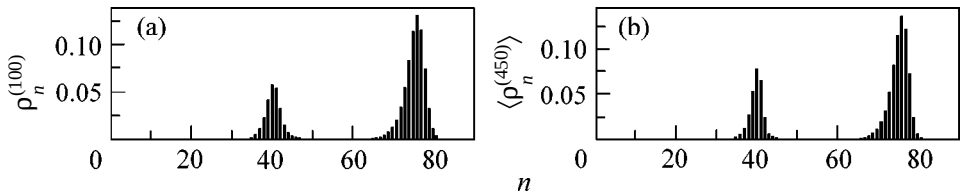

Fig. 3. The photon number distribution for $N_{ex} = 50$ and $n_b = 0.054$. At zero time, the field is in thermal equilibrium with the reservoir. (a) The mean number of atoms in the cluster is 15, and the number of passed clusters is 100. The distribution of atoms in the cluster is Gaussian with standard deviation of 3 atoms. (b) The cluster contains $N = 15$ atoms, and the number of passes is 450.

different. It is important to note that the width and position of the QTS remain virtually unchanged, as compared to the ideal case. From the facts listed above, it follows that an *N*-atomic micromaser can be used as a generator of stable sub-Poisson radiation.

In conclusion, note that this study allowed the revelation of a number of physical effects, which either appear only slightly or are absent in the one-atomic model. The proposed approach generalizes the basic model of a one-atomic micromaser and seems to be experimentally realizable. In this study, we pointed out the importance of the spectrum regions that are close to zero and responsible for the fast processes and the spectrum regions that are close to unity and related to the quasi-trapped states governing the quasi-equilibrium states.

I.P.V. is supported by the St. Petersburg's Individual Grant for Students and Young Specialists.

REFERENCES

1. S. Haroche and D. Kleppner, Phys. Today **42** (1), 24 (1989).
2. D. Meschede, H. Walther, and G. Müller, Phys. Rev. Lett. **54**, 551 (1985); G. Rempe, M. Scully, and H. Walther, Phys. Scr. **34**, 5 (1991); G. M. Brune, J. Raimond, P. Goy, *et al.*, Phys. Rev. Lett. **59**, 1899 (1987).
3. P. Filipowicz, L. Javanainen, and P. Meystre, Phys. Rev. A **34**, 3077 (1986).
4. P. Meystre and M. Sargent III, *Elements of Quantum Optics* (Springer-Verlag, Berlin, 1990).
5. P. Elmfors, B. Lautrup, and B. Shagerstam, Phys. Rev. A **54**, 5171 (1996).
6. P. Meystre, G. Rempe, and H. Walther, Opt. Lett. **13**, 1078 (1988).
7. G. D'Ariano, N. Sterpi, and A. Zuchetti, Phys. Rev. Lett. **74**, 900 (1995).
8. K. An, J. J. Childs, R. R. Dasari, and M. S. Feld, Phys. Rev. Lett. **73**, 3375 (1994).
9. M. Tavis and E. Cummings, Phys. Rev. **170**, 379 (1968); M. Scully, G. Meyer, and H. Walther, Phys. Rev. Lett. **76**, 4144 (1996).
10. A. Rybin, G. Kastelewicz, J. Timonen, and N. Bogoliubov, J. Phys. A **31**, 4705 (1998).
11. I. Vadeiko, G. Miroshnichenko, A. Rybin, and Yu. Timonen, Opt. Spektrosk. **89**, 328 (2000) [Opt. Spectrosc. **89**, 300 (2000)].
12. P. Filipowicz, J. Javanainen, and P. Meystre, J. Opt. Soc. Am. B **3**, 906 (1986); P. Meystre, G. Rempe, and H. Walther, Opt. Lett. **13**, 1078 (1988); O. Benson, G. Raithel, and H. Walther, Phys. Rev. Lett. **72**, 3506 (1994); M. Weidinger, B. T. H. Varcoe, R. Heerlein, and H. Walther, Phys. Rev. Lett. **82**, 3795 (1999).
13. M. Orszag, R. Ramírez, J. Retamal, and C. Saavedra, Phys. Rev. A **49**, 2933 (1994); L. Ladrón de Guevara, M. Orszag, and R. Ramírez, Phys. Rev. A **55**, 2471 (1997); M. Kolobov and F. Haake, Phys. Rev. A **55**, 3033 (1997).

Translated by R. Tyapaev

JETP Letters, Vol. 72, No. 9, 2000, pp. 453–456. Translated from Pis'ma v Zhurnal Éksperimental'noĭ i Teoreticheskoĭ Fiziki, Vol. 72, No. 9, 2000, pp. 653–657.

Compression of Terahertz Radiation in Resonant Systems with a Quantum Superlattice

A. A. Zharov[1], E. P. Dodin, and A. S. Raspopin

Institute of Physics of Microstructures, Russian Academy of Sciences, Nizhni Novgorod, 603600 Russia

[1] *e-mail: zharov@ipm.sci-nnov.ru*

Received August 3, 2000; in final form, October 2, 2000

It is shown theoretically that ultrashort terahertz electromagnetic pulses can be generated in resonant systems containing a quantum semiconductor superlattice. This effect is due to the compression of radiation incident on a cavity as a result of ultrafast self-modulation of the cavity Q factor upon cyclic switching of the superlattice from the screening to the transparent state in a pump field. *© 2000 MAIK "Nauka/Interperiodica".*

PACS numbers: 78.66.-w; 42.65.Pc

1. At present, considerable interest is reviving in the interaction of intense electromagnetic radiation with quantum semiconductor superlattices—semiconductor structures with chemical composition periodically changing on the nanometer scale [1–3]. The energy spectrum of charge carriers splits in the corresponding additional potential into a set of allowed and forbidden narrow (with widths of ~10–100 meV) minibands. Technological advances allow the fabrication of highly perfect superlattices (SLs) with a clearly defined miniband structure possessing, because of the narrow minibands, pronounced nonlinear properties in terahertz electromagnetic fields [4]. As a result, there is a real prospect of utilizing quantum SLs as highly efficient frequency multipliers, logic elements, amplifiers, and radiation sources in terahertz microelectronics.

In an external ac electromagnetic field, semiconductor SLs demonstrate a number of interesting nonlinear effects caused by the essentially nonparabolic dispersion law of electrons in a miniband. In particular, it is well known [5, 6] that, in a harmonic electric field directed along the SL axis, the dynamic electron localization effect occurs in the limit of relatively low frequencies of elastic and inelastic collisions. This effect arises when the $eEd/\hbar\omega$ parameter coincides with the roots of the Bessel function, $J_0(eEd/\hbar\omega) = 0$, where E and ω are, respectively, the amplitude and the frequency of the ac electric field, d is the SL spacing, e is the electron charge, and $\hbar$ is the Planck constant. Under conditions of dynamic localization, the ac currents turn to zero for all harmonics, for which reason the SL behaves as a linear dielectric transparent to the monochromatic electromagnetic radiation. This phenomenon has come to be known as self-induced transparency. However, recent self-consistent studies of the self-induced transparency of lateral SLs have shown [7] that the theory with an externally prescribed field incident on SL adequately describes nonlinear reflection of an electromagnetic wave only if the electron concentration is comparatively low, such that $\omega_p \ll \omega$, where ω_p is the electron plasma frequency at the miniband bottom. It was also shown that, if the electron concentration is sufficiently high to provide virtually ideal screening of radiation in weak fields, the bleaching regime occurs jumpwise[1] upon exceeding some critical value by the amplitude of the incident wave and is associated with attaining a bi- or multistable SL state under the action of nonlinear screening current flowing in the SL. This, in fact, signifies that the relationship between the electric field in the SL and the field of an incident pump wave is not uniquely defined. In this case, the self-consistent field in the SL contains higher harmonics, even if the incident wave is monochromatic, and the contribution of these harmonics to the electron transport processes may be significant, so that complete electron localization may not occur. The transmittance of a plane monochromatic electromagnetic wave incident normally on a lateral SL (the electric field vector is oriented along the SL axis) placed on a dielectric substrate is shown in Fig. 1 (taken from [7]) as a function of the amplitude of an incident high-frequency electric field. The bleaching of heavily doped SLs in intense electromagnetic fields is characterized by a short time of the respective transient processes which are indicated in Fig. 1 by arrows. This time is dictated by the electron

[1] The case at hand is the steady-state problem, where the reflection characteristics of the SL are determined after a lapse of time that is sufficient for the completion of all transient processes; in this case, the reflectance and transmittance can depend on the amplitude of the incident wave in a jumpwise manner.

0021-3640/00/7209-0453$20.00

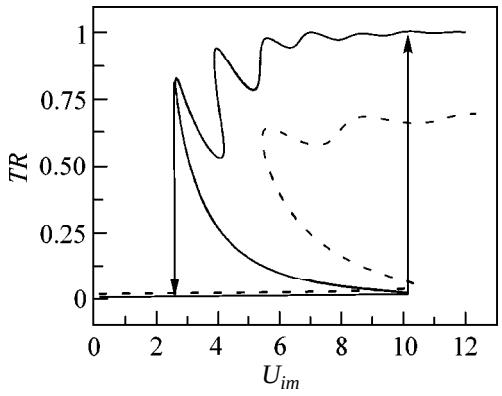

Fig. 1. Transmittance *TR* of an electromagnetic wave transmitting through the lateral SL placed on a dielectric substrate with permittivity ε_s vs. the amplitude of the incident high-frequency field; $\nu_1 = \nu_2 = 0.03$, and $\theta_0 = 30$ (see text for the notations). The solid line is for $\varepsilon_s = 1$, and the dashed line is for $\varepsilon_s = 12.4$.

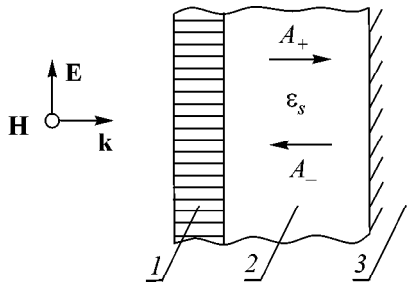

Fig. 2. Geometry of the problem: (*1*) quantum lateral superlattice; (*2*) dielectric medium with permittivity ε_s; and (*3*) ideal conductor. $A_{+,-}$ symbolize the partial waves in the cavity.

concentration, which determines the main (radiative) energy loss mechanism in this situation, and by the radiation intensity, which specifies another characteristic time scale for the system, viz., the Bloch frequency. In the circumstances considered in [7], the transient period was comparable to the period of a wave incident on the SL.

The main idea of this study is that the phenomenon of ultrafast SL switching from the screening to the transparent state is utilized for cavity Q-switching (SL may serve as one of the cavity mirrors) with the aim of generating ultrashort pulses via the energy accumulated in the cavity (the radiation compression effect). This work is devoted to studying the possibility of generating short pulses in a system with the unstable steady-state interaction between the pump wave and a cavity containing SL. As a result, the system finds itself in a dynamic self-modulation regime of reflection of the incident intense monochromatic wave, when slow energy accumulation by a cavity with an SL in the screening state is followed by fast field emission upon switching the SL to the transparent state.

2. As a starting physical model, we consider a one-dimensional dielectric Fabry–Perot cavity irradiated from vacuum by a plane electromagnetic wave. One of the cavity mirrors is formed by the lateral SL and the other is made from an ideal conductor (Fig. 2). The equations describing the nonlinear regime in such a system have a very simple form and, at the same time, allow the behavior of cavities of other types to be qualitatively studied because of the similarity of their properties. As in [7], the semiconductor SL, because of its small thickness, will be treated as an effective current screen and electron transport will be described using the constitutive equations derived in a single- miniband quasiclassical approximation:

$$\begin{aligned} dV/dt &= eE/m(W) - \nu_V V, \\ dW/dt &= eEV - \nu_W(W - W_T), \end{aligned} \tag{1}$$

where V and W are the mean (hydrodynamic) electron velocity and energy, respectively; ν_W is the frequency of inelastic collisions; $\nu_V = \nu_W + \nu_{el}$ is the velocity relaxation rate (ν_{el} is the frequency of elastic collisions); $m(W) = m_0/(1 - 2W/\Delta)$; $m_0 = 2\hbar^2/\Delta d^2$ is the electron effective mass at the miniband bottom; $W_T = (\Delta/2)(1 - \mu_0)$ is the electron mean thermal energy in the absence of the electric field; $\mu_0 = I_1(\Delta/2kT_0)/I_0(\Delta/2kT_0)$; Δ is the miniband width; T_0 is temperature; k is the Boltzmann constant; and I_0 and I_1 are the modified Bessel functions. The first of these equations is the equation of motion of an electron gas in a miniband with sine-shaped dispersion, and the second equation is the energy law. Using the d'Alembert solution for the one-dimensional wave equation in vacuum and in a cavity and inserting it into the boundary conditions for electric and magnetic fields at the current screen (SL) and the ideal conductor, one arrives at the following set of nonaveraged equations completely describing the dynamics of nonlinear interaction between the incident electromagnetic wave (generally, of an arbitrary time-dependent form) and the cavity of interest:

$$\begin{aligned} &d\nu/dt = U(1 - \zeta) - \nu_1 V, \quad d\zeta/dt = U\nu - \nu_2\zeta, \\ &2U_i(t) = (\sqrt{\varepsilon_s} + 1) f_+(t) + (\sqrt{\varepsilon_s} - 1) f_-(t) + \theta_0\nu(t), \end{aligned} \tag{2}$$

where $U_i(t) = U_{im}\cos\omega t$ is the electric field of the incident wave; $U = f_+ - f_-$; $f_{+,-} = f(t \pm \tau_0)$ are the electric fields of the partial waves in the cavity at the SL site; $\theta_0 = \mu_0(\omega_p^2/\omega^2)(\omega h/c)$; $\tau_0 = (\omega l/c)\sqrt{\varepsilon_s}$ is the dimensionless travel time from mirror to mirror for radiation in the cavity; h is the SL thickness; l is the distance between the mirrors; ε_s is the dielectric constant of a medium in the cavity; and c is the velocity of light in

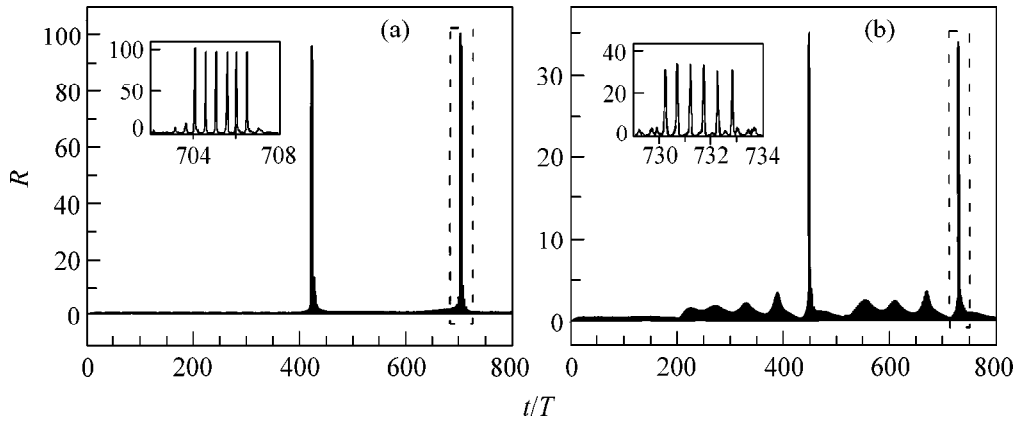

Fig. 3. Oscillograms of the reflected radiation intensity normalized to the intensity of the wave incident on the cavity. The time is measured in periods of the incident wave. (a) $\varepsilon_s = 1.0$, $U_{im} = 1.8$, $n = 3$ and (b) $\varepsilon_s = 12.4$, $U_{im} = 1.8$, $n = 3$.

free space. In Eqs. (2), the variables are normalized in the following way:

$$U = \frac{ed}{\hbar\omega}E, \quad \nu = \frac{2\hbar}{\Delta d\mu_0}, \quad \zeta = \frac{2(W - W_T)}{\Delta\mu_0},$$

$$t = \omega t, \quad \nu_1 = \frac{\nu_V}{\omega}, \quad \nu_2 = \frac{\nu_W}{\omega}.$$

The solution of the set of Eqs. (2) was analyzed on a computer. Numerical simulation showed that, as the electron concentration exceeds some critical value (corresponding to $\theta_0 \sim 5$), the system occurs in a bistable state and the self-modulation dynamic reflection regime occurs under conditions close to those for linear matching of the incident radiation and the cavity,

$$\tan(\tau_0) = -\sqrt{\varepsilon_s}\nu_1, \quad \theta_0 = \nu_1 + 1/\nu_1. \qquad (3)$$

This process is characterized by a relatively slow energy accumulation in the cavity followed by a rapid (in a time close to the time of radiation travel from mirror to mirror) emission to form a quasi-periodic sequence of short reflected pulses. Figure 3 demonstrates typical oscillograms for the normalized (to the intensity of incident wave) intensity of the field reflected from the cavity (dynamic reflectance). The calculations were carried out with the following parameters: $\varepsilon_s = 1$ and 12.4 (GaAs); $\omega = 2 \times 10^{13}$ s^{-1}; $\nu_V = \nu_W = 10^{12}$ s^{-1} ($\nu_{el} = 0$); $h = 10^{-5}$ cm; $\theta_0 = 30$ (the corresponding electron concentration $n_e \sim 7 \times 10^{17}$ cm^{-3}); $d = 10^{-6}$ cm; and $T_0 = 300$ K. The spectral composition of the reflected radiation is dictated by the cavity volume. After switching the SL from the screening to the bleached state, the energy accumulated in the cavity is emitted in the form of a sequence of short pulses, whose number in the group is determined by the number n of electric field variations in the cavity eigenmode and is equal to $2n$. The fine structure of each pulse sequence is shown in the insets in Fig. 3. In dimensionless variables, the total duration of each group is $T_g \sim 2\tau_0$ and the duration of an individual peak is $T_p \sim \tau_0/n$. For the chosen high-Q cavities, the τ_0 value corresponds to the situation when the cavity length is approximately divisible by a half-wave [see Eq. (3)]; i.e., $\tau_0 \sim n\pi$ in dimensionless units. Therefore, the peak duration in this case is equal to $\sim\pi$, which corresponds, in time units, to ~150 fs for $\varepsilon_s = 1$. For the self-modulation regime to be developed under the indicated conditions, the radiation intensity incident on the SL should exceed $S_i \approx 5 \times 10^3$ W/cm^2. The peak intensity of the pulse was as high as $S_{\max} \approx 4 \times 10^5$ W/cm^2, which corresponds to an intensity gain of nearly two orders of magnitude. Note also that a decrease (even rather considerable) in the cavity Q-value with decreasing electron concentration in the SL or increasing collision frequency does not bring about quenching of the generation of short pulses, as long as bi(multi)stability occurs in the system, and virtually does not affect the threshold intensity of incident radiation. Only the peak amplitude of the reflected pulse decreases with decreasing Q value.

3. In summary, a very simple one-dimensional model of a Fabry–Perot cavity containing a quantum semiconductor lateral SL as a mirror and illuminated from vacuum by a terahertz monochromatic wave was invoked in this work to demonstrate the possibility of generating femtosecond electromagnetic pulses. The SL parameters used in the calculations are quite attainable with modern technologies [8], while the necessary radiation characteristics are already realized on setups of the FEL type [4].

This work was supported by the Russian Foundation for Basic Research (project no. 99-02-17956) and the program “Physics of Solid Nanostructures” (project no. 99-1129).

REFERENCES

1. A. A. Ignatov, E. Schomburg, J. Grenzer, *et al.*, Z. Phys. B **98**, 187 (1995).
2. A. A. Ignatov and A. P. Jauho, J. Appl. Phys. **85**, 3643 (1999).
3. C. Cao, H. C. Liu, and X. L. Lei, Phys. Rev. B **61**, 5546 (2000).
4. M. L. Wanke, S. J. Allen, K. Maranowski, *et al.*, in *Physics of Semiconductors*, Ed. by M. Scheffter and R. Zimmerman (World Scientific, Singapore, 1997), p. 1791.
5. A. A. Ignatov and Yu. A. Romanov, Phys. Status Solidi B **73**, 327 (1976).
6. D. H. Dunlap and V. M. Kenkre, Phys. Rev. B **34**, 3625 (1986).
7. E. P. Dodin, A. A. Zharov, and A. A. Ignatov, Zh. Éksp. Teor. Fiz. **114**, 2246 (1998) [JETP **87**, 1226 (1998)].
8. H. Noguchi, J. P. Leburton, and H. Sakaki, Inst. Phys. Conf. Ser., No. 129 (5), 299 (1993).

Translated by V. Sakun

JETP Letters, Vol. 72, No. 9, 2000, pp. 457–459. From Pis'ma v Zhurnal Éksperimental'noĭ i Teoreticheskoĭ Fiziki, Vol. 72, No. 9, 2000, pp. 658–661.

Laser Writing of a Subwavelength Structure on Silicon (100) Surfaces with Particle-Enhanced Optical Irradiation[1]

Y. F. Lu[1], L. Zhang[1], W. D. Song[1], Y. W. Zheng[1], and B. S. Luk'yanchuk[2,3]

[1] *Laser Microprocessing Lab., Department of Electrical Engineering, Data Storage Institute National University of Singapore, 119260 Singapore*

[2] *On leave from the Wave Research Center, Institute of General Physics, ul. Vavilova 38, Russian Academy of Sciences, Moscow, 117942 Russia*

[3] *e-mail: boris@dsi.nus.edu.sg*

Received October 9, 2000

Spherical 0.5-μm silica particles were placed on a silicon (100) substrate. After laser illumination with a 248-nm KrF excimer laser, hillocks with size of about 100 nm were obtained at the original position of the particles. The mechanism of the formation of the subwavelength structure pattern was investigated and found to be the near-field optical resonance effect induced by particles on the surface. Theoretically calculated near-field light intensity distribution was presented, which was in agreement with the experimental result. The method of particle-enhanced laser irradiation has potential applications in nanolithography. © *2000 MAIK "Nauka/Interperiodica"*.

PACS numbers: 42.82.Cr; 85.40.Hp

The field of nanoelectronics has evolved into a major area of investigation. Nanolithographic techniques such as atom beams [1, 2], electron beams [3], scanning probe tunneling [4–6], and scanning near-field optical lithography [7–9] are expected to be potential methods in the fabrication of present and future nanodevices. However, due to their incompatibility with the present fabrication processing and their low throughput, the application of these methods is presently confined to the experimental stage. Meanwhile, traditional optical lithography is limited to the diffraction effect and always relates to complex system and high cost. In this letter, we report a novel, low-cost, and simple optical lithography technique using particle-enhanced laser irradiation.

Standard spherical silica particles (Duke [10]) packaged as low-residue aqueous suspensions were used in our experiment. The diameter of the particles is 0.5 μm, with a deviation limited in a range of ±5%. Silicon (100) samples were dipped in 5% hydrofluoric acid for 20 seconds of hydrogen passivation and rinsed with DI water afterwards. Particles were applied on Si (100) surfaces and dried by a hot air jet. The location of the particles on the substrate before laser irradiation was observed with an optical microscope. As shown in Fig. 1a, the particles are spherical and smooth and many of them are free of aggregation.

A 248-nm KrF excimer laser with pulse duration of 23 ns was used. In order to produce an observable laser-induced pattern, beam intensity in the area of the sample was adjusted to about 340 mJ/cm^2. The laser beam was incident normally on the Si (100) surface. The pulse number was 200. The sample, after laser irradiation, was observed again with the optical microscope, as shown in Fig. 1b. Comparison of the two pictures, i.e., before and after irradiation, showed that localized black spots (Fig. 1b) appeared at the original position of the particles (Fig. 1a). In the two pictures, the original particle position (Fig. 1a) and the observed corresponding black spots (Fig. 1b) are marked by curves.

Field-emission SEM was used to track the black spots that corresponded to the original particle position. The SEM image (Fig. 2a) shows the black spot observed in Fig. 1 as a circular hillock, and a curve around the hillock can be clearly seen. This curve around the hillock can also be seen in Fig. 2b, the AFM observation. This indicates that the hillocks were produced due to melting of the "hot point." The size of the hillock is about 100 nm, with height about 10 nm.

The same laser fluence (340 mJ/cm^2) was also applied on clean Si (100) surfaces (without particles), but no damage spots were observed. It is obvious that higher intensity was achieved due to the spherical particles in our experiment, and this resulted in the formation of the hillocks. The mechanism can be explained as the enhancement of light intensity near the contact area [11–13]. Since the characteristic distance between particles and substrate is smaller than the radiation wave-

[1] This article was submitted by the authors in English.

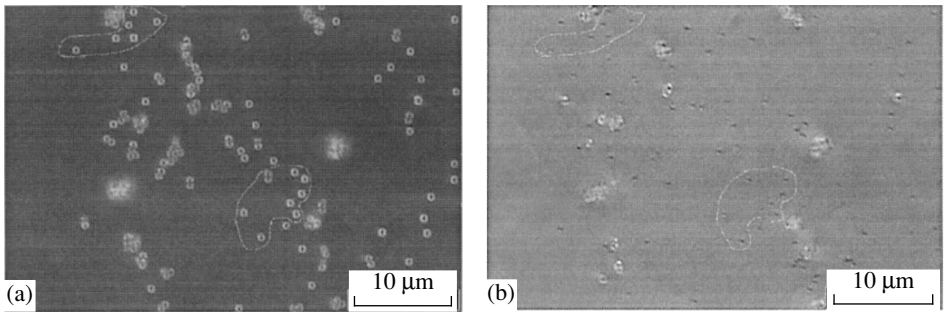

Fig. 1. Optical microscope observation of the localized hillocks induced by particle-enhanced laser irradiation: surface view (a) before and (b) after irradiation.

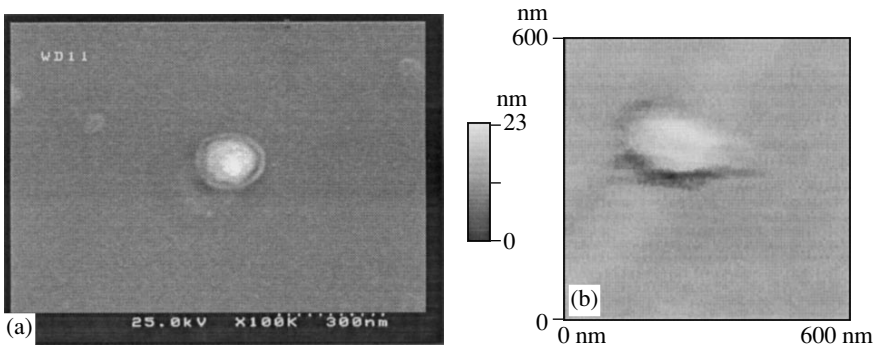

Fig. 2. Image of the hillock structure: (a) SEM and (b) AFM. These pictures present different hillocks.

length, and the particle size is of the order of a wavelength, particles do not simply play the role of microfocusing lens as in far-field, but relate to the optical resonance effect in near-field. The source of the optical resonance is excitation of partial waves (multipole modes of a spherical cavity) [14]. The optical resonance produces a high-intensity zone in the near-field region, and, naturally, when this high-intensity zone is on the substrate surface, it can lead to formation of "hot points."[1] These "hot points" produced the hillocks.

The light intensity on the surface under the spherical particle was calculated by solving the electromagnetic boundary problem "particle on surface" [12, 15, 16]. "Mathematica-4" [17] was used for calculations. Figure 3 shows the intensity distribution within the plane perpendicular to the wave vector of the incident wave. This intensity I is defined as the normalized value of the z-component of the time-averaged Poynting vector. From the picture, a strong optical enhancement can be seen. The intensity of light in the center is 20 times greater than the incident intensity. The achievement of the higher intensity according to calculations was clearly observed in our experiment. This computational result can also explain the work done by Kane and Halfpenny [18], in which the damage threshold of glass substrates was reduced by smaller surface particle coverage. The full width at half maximum (FWHM) in the intensity distribution is shown in Fig. 3. The FWHM is equal to 80 nm, which agrees with the hillock size of 100 nm. This confirmed that a subwavelength structure was achieved in our experiment.

The small nanoparticles have potentially useful optical, optoelectonic, and material properties that might lead to application in nanostructure fabrication [19]. Although the 0.5 μm (submicron) spherical particles discussed in the present paper work by a different mechanism, they too have the same potential in nanofabrication by producing enhanced light intensity in the near field. Further theoretical calculation shows that even higher line resolution below 100 nm can be achieved by selecting a suitable particle size and wavelength. We do not discuss here the technical problem related to particle arrangement and positioning.

In conclusion, we have reported a novel lithographic technique where particles were applied on a silicon surface and a subwavelength structure was achieved with particle-enhanced laser irradiation. The mechanism was found to be the near-field optical resonance effect induced by particles on the surface. Calculation result was presented by solving the electromagnetic boundary problem. Compared to other nanolithographic techniques, the method of particle-enhanced laser irradiation does not need a complex system and uses neither a

[1] It follows from the Mie theory calculations [11–13], as well as from more precise calculations [12], which take into account the secondary scattering of radiation reflected by the substrate.

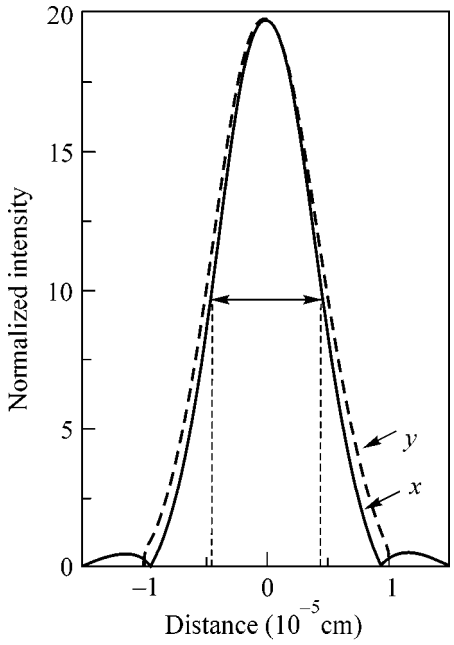

Fig. 3. The light intensity distributions (*z*-component of the averaged Poynting vector) on the substrate surface under the spherical particle (calculations with the Mie theory). Vector **E** of the incident plane wave is directed along the *x* axis, vector **H** along the *y* axis. Distribution of the surface intensity along the *x* axis is shown by a solid line and along the *y* axis by a dashed line.

mask nor a resist, but simply relies on the near-field optical resonance effect to achieve higher resolution and intensity. Hence, it, may have greater potential in nanofabrication.

Addition: When this paper was ready for publication, we received information from the Konstanz and Madrid groups that they had also found a similar optical field-enhancement effect using shorter laser pulses (from 150 fs to 6.5 ns) [20].

The authors thank Dr. S.M. Huang, Ms. W.J. Wang and Mr. X.Y. Chen for their kind assistance in our experiment. The authors also thank Dr. Z.H. Mai (AMD, Singapore) for his contributions to our work. We are grateful to the authors of [20] for rapid information about their experiments. B.L. is grateful to Prof. S. Anisimov for discussions and to the people at the Data Storage Institute at National University of Singapore for their hospitality. This work was supported in part by the Russian Foundation for Basic Research project no. 98-02-16104.

REFERENCES

1. S. J. Rehse, A. D. Glueck, S. A. Lee, *et al.*, Appl. Phys. Lett. **71**, 1427 (1997).
2. A. S. Bell, B. Brezger, U. Drodofsky, *et al.*, Surf. Sci. **435**, 40 (1999).
3. S. Fujita, S. Maruno, H. Watanabe, and M. Ichikawa, Appl. Phys. Lett. **69**, 638 (1996).
4. J. A. Dagata, J. Schneir, H. Harary, *et al.*, Appl. Phys. Lett. **56**, 2001 (1990).
5. H. C. Day and D. R. Allee, Appl. Phys. Lett. **62**, 2691 (1993).
6. E. S. Snow and P. M. Campbell, Appl. Phys. Lett. **64**, 1932 (1994).
7. J. Jersch and K. Dickmann, Appl. Phys. Lett. **68**, 868 (1996).
8. S. Madsen, M. Mülleborn, K. Birkelund, and F. Grey, Appl. Phys. Lett. **69**, 544 (1996).
9. Y. F. Lu, Z. H. Mai, Y. W. Zheng, and W. D. Song, Appl. Phys. Lett. **76**, 1200 (2000).
10. Duke silica particles are supplied by Duke Sci. Corp.
11. Y. F. Lu, Y. W. Zheng, and W. D. Song, J. Appl. Phys. **87**, 1534 (2000).
12. B. S. Luk'yanchuk, Y. W. Zheng, and Y. F. Lu, Proc. SPIE **4065** (2000).
13. P. Leiderer, J. Boneberg, V. Dobler, *et al.*, Proc. SPIE **4065** (2000).
14. M. Kerker, *The Scattering of Light* (Academic, New York, 1969).
15. P. A. Bobbert and J. Vlieger, Physica A (Amsterdam) **137**, 209 (1986).
16. P. A. Bobbert, J. Vlieger, and R. Greef, Physica A (Amsterdam) **137**, 243 (1986).
17. S. Wolfram, *The Mathematica Book* (Wolfram Media, Champaign, 1999, 4th ed.).
18. D. M. Kane and D. R. Halfpenny, J. Appl. Phys. **87**, 4548 (2000).
19. C. A. Mirkin, R. L. Letsinger, R. C. Mucic, and J. J. Storhoff, Nature **382**, 607 (1996).
20. M. Mosbacher, H.-J. Munzer, J. Zimmermann, *et al.*, Appl. Phys. A (2000) (in press).

JETP Letters, Vol. 72, No. 9, 2000, pp. 460–463. Translated from Pis'ma v Zhurnal Éksperimental'noĭ i Teoreticheskoĭ Fiziki, Vol. 72, No. 9, 2000, pp. 662–667.

Dimensional Magnetoplasma Resonance of 2D Holes in (001) GaAs/AlGaAs Quantum Wells

M. Yu. Akimov[1], I. V. Kukushkin[1,2], S. I. Gubarev[1], S. V. Tovstonog[1], J. Smet[2], K. von Klitzing[2], and W. Wegscheider[3]

[1] *Institute of Solid State Physics, Russian Academy of Sciences, Chernogolovka, 142432 Russia*
e-mail: gubarev@issp.ac.ru
[2] *Max-Planck-Institut für Festkörperforschung, 70569 Stuttgart, Germany*
[3] *Walter Schottky Institute, Technische Universität München, Am Coulombwall, D-85748 Garching, Germany*

Received August 21, 2000; in final form, September 27, 2000

Dimensional magnetoplasma resonance is observed and studied in a spatially confined, two-dimensional hole system in (001) GaAs/AlGaAs single quantum wells. From the analysis of the field dependence of the magnetoplasma resonance on the diameter of the 2D system, the semiclassical cyclotron hole mass is determined. Its value is found to be equal to $0.26m_0$ (m_0 is the free electron mass), which considerably exceeds the theoretically predicted value. A method is proposed for a direct determination of the concentration and mobility of 2D holes from the analysis of the magnetoplasma resonance. © *2000 MAIK "Nauka/Interperiodica"*.

PACS numbers: 73.20.Dx; 73.50.Mx; 76.70.Hb

The size quantization in GaAs/AlGaAs-based heterostructures eliminates the fourfold degeneracy of the valence band and splits the hole states into two subbands with a twofold spin degeneracy by forming the so-called heavy and light hole subbands. The terms "heavy" and "light" subbands are determined by the longitudinal hole masses, which govern the size quantization energy of the hole states in a quantum well. The lowest energy state is the state of a heavy hole for which the size quantization energy is less, and the light hole subband lies at higher energies. The longitudinal masses of light and heavy holes are known, because just these quantities determine the size quantization energies of the hole states in a well, and the corresponding energies are reliably measured by different optical techniques. Much less data are available on the values of the hole masses in the well plane. According to the theoretical calculations performed by Ando [1] and Ekenberg [2] for single junctions and for quantum wells, the energy spectrum of 2D holes in GaAs heterostructures on the (001) surface is fairly complicated. These studies showed that, when k is nonzero, the repulsion of the light and heavy hole zones leads to a considerable nonparabolicity of the dispersion of heavy holes even for energies as low as several millielectronvolts. In this case, owing to the terms linear in k, the dispersion laws for the hole states with different spins are noticeably different. As a result, for the heavy hole states with different spins, the planar masses can differ severalfold. The situation is simplified for low concentrations of 2D holes. In this case, the dispersion laws become practically independent of the spin states of holes and a well-determined parameter comes into play, namely, the semiclassical heavy hole mass, which, according to the calculations, is equal to $m_h = 0.16m_0$ [1, 2]. However, until now, no experimental measurements of the planar hole mass had been performed for the case of low concentrations, when the effect of nonparabolicity can be neglected. In the studies of magnetoabsorption in the far infrared region [3, 4], it was only possible to measure the transitions between the lowest Landau levels in which the value of the cyclotron mass does not directly manifest itself. In addition, the experiments with infrared magnetoabsorption were performed on samples with high hole concentrations, so that not only did the effects of nonparabolicity substantially contribute to the measured quantity, but the transition energies for holes with different spins also differed several times.

The most reliable method of measuring the planar mass of the charge carriers is the cyclotron resonance method. Up to now, no data had been reported on the cyclotron resonance measurements in a GaAs/AlGaAs hole channel at the (100) surface in the microwave frequency range. The need for microwave cyclotron resonance measurements is determined by the fact that, because of the strong nonparabolicity of the hole dispersion, it is necessary to study the cyclotron transitions near the bottom of the hole band. In addition, only with the microwave studies, can one expect to measure the cyclotron transitions between the Landau levels with large numbers, as well as the quantity well defined

in the theory—the semiclassical cyclotron mass of the holes.

The difficulty in detecting the cyclotron resonance in the microwave region is related to the necessity of using samples with a very high mobility of 2D holes, because, in this case, the resonance is shifted to the region of low magnetic fields and the condition $\omega_c\tau > 1$ is fulfilled only for long momentum relaxation times. Unlike 2D electron channels in which sufficiently large values of τ can be obtained without any special problems, in 2D hole systems, high mobility can be achieved only for silicon-doped heterostructures grown on the (311) surface [4]. However, such structures exhibit a strong planar anisotropy of conductivity, which is absent in conventional quantum wells obtained on the (001) surface. The main difficulty in obtaining high-mobility *p*-type channels in (001) GaAs/AlGaAs quantum wells consists in the necessity to use beryllium for the *p*-type doping of the barrier, this substance being absent in the best MBE systems. In contrast to the conventional techniques used for obtaining *p*-type channels, in our experiments, we used *p*-type high-quality (001) GaAs/AlGaAs quantum wells in which the 2D hole channel was formed owing to the residual natural impurities (carbon) present in the barrier. The resulting concentration of 2D holes proved to be fairly low (~10^{10} cm^{-2}), but their mobility was found to reach record high values ((2–3) × 10^5 cm^2/V s) and satisfied the conditions for the observation of microwave cyclotron resonance.

It should be noted that the dispersion law of heavy holes in (001) GaAs/AlGaAs quantum wells should be known not only for studying the properties of 2D hole channels, but also for studying 2D electron systems by the optical methods that are based on analysis of the electron–hole recombination radiation.

In this paper, we present the results of the cyclotron resonance measurements for 2D holes in the microwave frequency range. The results were obtained by studying the dimensional magnetoplasma resonance for GaAs/AlGaAs heterostructures grown in the (100) direction.

The measurements were performed on high-quality GaAs/AlGaAs single quantum wells with widths 300 and 250 Å. To study the dimensional magnetoplasma resonance, special mesas were prepared on the sample surfaces. The mesas were made by etching in the form of disks with diameters 0.1, 0.2, 0.5, and 1 mm and thickness 500 nm. Their positions were selected so that the 2D channel was within such a mesa. The resulting structures were placed in a microwave channel (16 mm) at the antinode of the microwave electric field. The experiments were performed in the frequency range from 16 to 40 GHz at a temperature of $T = 1.5$ K. The microwave absorption was recorded by the method of optical detection, which was recently developed for studying the magnetoplasma resonance in 2D electron gas [5]. For this purpose, an optical fiber was connected to the sample, and this fiber was used for both optical excitation and recording the recombination radiation of the 2D hole gas. The radiation spectra were analyzed by a double spectrometer (which provided a resolution of 0.03 meV) and detected by a photomultiplier. The microwave radiation power was modulated at a frequency of 500 Hz, and the dependences of the synchronously detected luminescence signal on the radiation wavelength and on the magnetic field were studied.

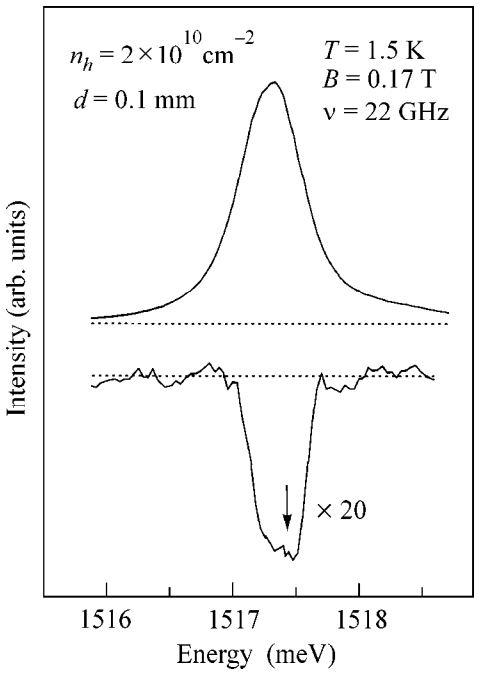

Fig. 1. Luminescence spectrum and the differential (with respect to the microwave power) radiation spectrum of the 2D hole gas. The spectra are measured in a (001) GaAs/AlGaAs quantum well 300 Å wide at $T = 1.5$ K in the resonance magnetic field $B = 0.17$ T for a mesa with diameter $d = 0.1$ mm in the case of the microwave excitation at a frequency of 22 GHz. The 2D hole concentration is 2×10^{10} cm^{-2}.

Figure 1 presents a typical luminescence spectrum of the 2D hole gas (the upper curve) and the corresponding differential (with respect to the microwave power) spectrum (the lower curve) recorded in the resonance magnetic field ($B = 0.17$ T for the frequency $f =$ 22 GHz). As one can see from this figure, in the case of a low-density hole channel, the resonance absorption of the microwave power leads to a decrease in the integral luminescence intensity. Such behavior is mainly related to resonance heating of the hole gas due to the microwave power absorption. The intensity, the spectral position, and the line shape of the recombination radiation of the 2D hole gas are practically independent of the magnetic field in the field range used in the experiment, $H \le 0.35$ T. Therefore, the dependence of the modulated luminescence signal (measured at the line maximum) on magnetic field represents the resonance profile of

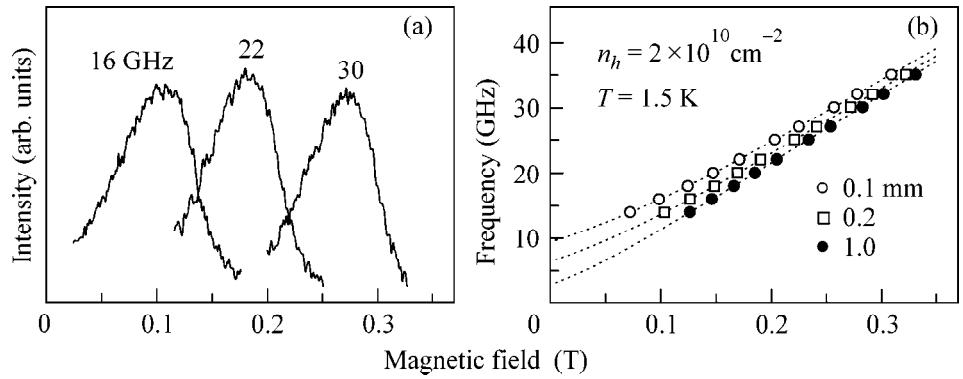

Fig. 2. (a) Profiles of the optically detected dimensional magnetoplasma resonance of the 2D hole gas for different microwave excitation frequencies for a mesa with diameter d = 0.1 mm in a (001) GaAs/AlGaAs quantum well 300 Å wide. The 2D hole concentration is 2×10^{10} cm^{-2}. (b) Field dependences of the optically detected dimensional magnetoplasma resonances for mesas with different diameters (d = 0.1, 0.2, and 1 mm) for a 2D hole channel of density 2×10^{10} cm^{-2}. The dotted lines show the approximations obtained by Eq. (1) for the upper branch of the magnetoplasma mode.

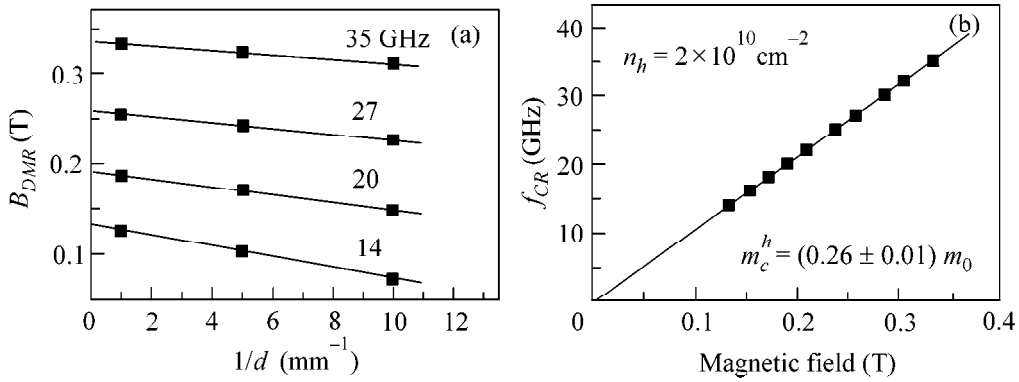

Fig. 3. (a) Dependences of the resonance magnetic field on the inverse diameter of the mesa for several microwave excitation frequencies. (b) Magnetic field dependence of the cyclotron contribution to the magnetoplasma resonance frequency in Eq. (1). The dependence is measured in the (001) GaAs/AlGaAs quantum well 300 Å wide with the concentration 2×10^{10} cm^{-2}. The straight line corresponds to the cyclotron hole mass in the well plane, $m_c^h = 0.26 m_0$.

the microwave absorption by 2D holes to a high degree of accuracy.

Figure 2a illustrates the changes that occur in the position and shape of the resonance microwave absorption (the dependence of the differential intensity of luminescence on magnetic field) with the variation of the microwave excitation frequency. One can see that a decrease in the microwave excitation frequency leads to a shift of the resonance peak toward lower magnetic fields, while the width of the resonance curve is practically unchanged. The width of the resonance is determined by the elastic scattering time of 2D holes, and, hence, their mobility can be determined from analysis of the resonance curve.

As in 2D electron systems [6], the limited dimensions of the samples lead to mixing of the plasma and cyclotron modes and to a dependence of the resonance frequency on both the concentration of 2D charge carriers and the dimensions of the structure [5, 7]. For a structure in the form of a disk with diameter d, we obtain the following expression for the frequencies of the upper and lower magnetoplasma branches:

$$\omega_{DMR} = \pm\frac{\omega_{CR}}{2} + \sqrt{\omega_p^2 + \left(\frac{\omega_{CR}}{2}\right)^2}, \qquad (1)$$

where $\omega_{CR} = eH/m^*c$ is the cyclotron frequency and $\omega_p^2 = 3\pi^2 n_{2D} e^2/2m^*\epsilon_{\text{eff}} d$ is the plasma frequency of 2D carriers with the concentration n_{2D} in a mesa of diameter d; here, $\epsilon_{\text{eff}} = (1 + \epsilon_0)/2$ is the average dielectric constant of vacuum and GaAs.

Figure 2b shows the resonance magnetic field dependence measured for the upper branch of the optically detected dimensional magnetoplasma resonance for different microwave excitation frequencies and mesas of different diameters at a fixed concentration of holes. From this figure, one can see that, in the case of

the greatest diameter (d = 1 mm), the dependence of the resonance frequency on magnetic field is close to linear. This is related to the fact that the plasma energy decreases with increasing d as $d^{-1/2}$ and its contribution to the energy of the hybrid magnetoplasma mode becomes small compared to the cyclotron energy. As the diameter of the mesa decreases, the plasma frequency increases, which leads to a shift of the resonance absorption maximum to lower magnetic fields (at a fixed microwave excitation frequency) in compliance with Eq. (1). For the shift of the resonance field B_{DMR} of the upper branch of the dimensional magnetoplasma resonance relative to the resonance field of the cyclotron resonance B_{CR} at a fixed microwave excitation frequency f, we can write the expression

$$B_{DMR} = B_{CR} - 3\pi ecn_{2D}/4f\varepsilon_{\text{eff}}d. \quad (2)$$

Figure 3a presents the experimental dependences of the resonance magnetic field on the inverse diameter of the mesa for different microwave excitation frequencies f. According to Eq. (2), the slope of these linear dependences is determined by the microwave excitation frequency and by the concentration of 2D charge carriers. This allowed us to determine the hole concentration, which was found to be 2×10^{10} cm^{-2}. The mobility of the 2D holes at this concentration value could be determined from the width of the resonance curve, and it proved to be 2×10^5 cm^2/V s. To determine the semiclassical cyclotron mass of 2D holes, it is necessary to separate the cyclotron and plasma contributions to the energy of the magnetoplasma mode. From Eq. (2), it follows that, since the contribution of the plasma frequency decreases as the diameter of the mesa increases, we can eliminate the plasma contribution by approximating the dependence of the resonance magnetic field on the diameter for the case $1/d \longrightarrow 0$ (which corresponds to the case of a structure of infinite dimensions). Thus, we can determine the value of the resonance magnetic field corresponding to a given cyclotron frequency. Figure 3b shows the dependence of the cyclotron frequency on magnetic field, this dependence being measured by the aforementioned method for the 2D hole concentration 2×10^{10} cm^{-2}. One can see that this dependence is adequately described by a linear function whose slope corresponds to the effective cyclotron mass $m_h = 0.26m_0$. The measured value of the semiclassical cyclotron mass of holes noticeably differs from the value calculated theoretically [1, 2], which means that the computational model requires some modification.

Thus, we have experimentally measured the cyclotron mass of 2D holes in a (001) GaAs/AlGaAs quantum well. The study of the dimensional magnetoplasma resonance in the microwave frequency range allows one to determine the concentration of the holes in the channel and their effective elastic scattering time.

This work was supported by the Russian Foundation for Basic Research, the program "Physics of Solid Nanostructures," and the INTAS (project no. 99-1146).

REFERENCES

1. T. Ando, J. Phys. Soc. Jpn. **54**, 1528 (1985).
2. U. Ekenberg and M. Altarelli, Phys. Rev. B **32**, 3712 (1985).
3. H. L. Stormer, Z. Schelesinger, A. Chang, *et al.*, Phys. Rev. Lett. **51**, 126 (1983).
4. B. E. Cole, J. M. Chamberlain, M. Henini, and T. Cheng, Phys. Rev. B **55**, 2503 (1997).
5. B. M. Ashkinadze *et al.*, Phys. Status Solidi A **164**, 523 (1997).
6. S. I. Gubarev, I. V. Kukushkin, S. V. Tovstonog, *et al.*, Pis'ma Zh. Éksp. Teor. Fiz. **72**, 469 (2000) [JETP Lett. **72**, 324 (2000)].
7. S. J. Allen, H. L. Stormer, and J. C. M. Hwang, Phys. Rev. B **28**, 4875 (1983).

Translated by E. Golyamina

JETP Letters, Vol. 72, No. 9, 2000, pp. 464–467. Translated from Pis'ma v Zhurnal Éksperimental'noĭ i Teoreticheskoĭ Fiziki, Vol. 72, No. 9, 2000, pp. 668–672.

Heat Capacity and Resistivity of $Sm_{0.55}Sr_{0.45}MnO_3$ in Magnetic Fields of up to 26 kOe

A. M. Aliev[1,2], Sh. B. Abdulvagidov[1,2], A. B. Batdalov[1,2], I. K. Kamilov[1,2], O. Yu. Gorbenko[3], and V. A. Amelichev[3]

[1] *Institute of Physics, Dagestan Scientific Center, Russian Academy of Sciences, ul. 26 Bakinskikh Komissarov 94, Makhachkala, Dagestan, 367003 Russia*

[2] *e-mail: lowtemp@datacom.ru*

[3] *Moscow State University, Vorob'evy gory, Moscow, 119899 Russia*

Received August 28, 2000; in final form, September 28, 2000

Heat capacity and resistivity of $Sm_{0.55}Sr_{0.45}MnO_3$ ceramics were measured over the temperature range 80–300 K in magnetic fields of up to 26 kOe. These quantities show anomalies caused by the magnetic and structural phase transitions. The critical temperature T_c and the heat capacity jump $\Delta C_p(T_c)$ at T_c increase with increasing applied magnetic field H, while the resistivity decreases. The temperature dependences of the measured quantities show hysteresis, which is strongly suppressed in a field of 26 kOe but is sensitive nor to the temperature range neither to the rate of temperature change. The hysteresis of the heat capacity and resistivity of $Sm_{0.55}Sr_{0.45}MnO_3$ is caused by a change in T_c with changing lattice parameters upon second-order structural phase transition. The results are discussed in terms of the electron phase separation model. © *2000 MAIK "Nauka/Interperiodica".*

PACS numbers: 75.30.Vn; 75.40.Cx; 65.40.+g

Persistent interest in partly substituted $Ln_{1-x}A_xMnO_3$ manganates, where Ln is a rare-earth element and A is a bivalent alkaline-earth metal, is due to the discovery of the colossal magnetoresistance (CMR) effect in these materials. In spite of recent extensive studies, a unified point of view on the nature of the anomalous properties of manganates is as yet lacking. For usual magnetic semiconductors, the CMR effect is explained by the presence of a strong indirect exchange and ensuing two-phase magnetic state. The situation in manganates is more intricate because of the presence of the Jahn–Teller effect and a comparative softness of the lattice, for which reason the crystal structure is amenable to the action of temperature, magnetic field, or pressure. To interpret the unusual properties of manganates, several models are invoked, among which are crossover from polaron conduction to hopping transport at T_c, melting of the charge-ordered state in a magnetic field, etc. (see, e.g., reviews [1, 2]). However, these models fail to account for all available experimental results. In recent years, much evidence has been obtained favoring the existence of a two-phase magnetic state in manganates [3–5]. The ferromagnetic metal (FM) and the antiferromagnetic dielectric (AFD) phases can also coexist in the $Sm_{1-x}Sr_xMnO_3$ compounds [6, 7]. At $x = 0.45$, the magnetic and structural phase transitions occur simultaneously [7, 8], rendering this compound suitable for studying the topical problem of interplay between the electronic, magnetic, and phonon subsystems of manganates. The purpose of this study was to make a further contribution to the understanding of the nature of CMR and fill the gap associated with the lack of experimental data on the heat capacity and resistivity of $Sm_{0.55}Sr_{0.45}MnO_3$ in magnetic fields.

The $Sm_{0.55}Sr_{0.45}MnO_3$ ceramic was prepared by the chemical homogenization method through mixing stoichiometric amounts of aqueous solutions of Sm, Sr, and Mn nitrates. The resulting solution with a total metal concentration of 1 mol/l was used for the impregnation of benzene filters, which were dried and burned out. After 30 min of annealing at 700°C, the formed powder was pelleted and sintered at 1200°C for 16 h. According to the X-ray diffraction data, the ceramic was a single-phase orthorhombic perovskite with lattice parameters $a = 0.5424(1)$, $b = 0.7678(2)$, and $c = 0.5434(2)$ nm. Scanning electron microscopy showed that the ceramic had a homogeneous granulometric structure with the average grain size of 2 μm, tight sintering, and a porosity of about 20%. X-ray spectroscopic microanalysis suggested that the granules were chemically uniform and had the $Sm_{0.55}Sr_{0.45}MnO_3$ com-

0021-3640/00/7209-0464$20.00

position. The oxygen stoichiometric index was determined by iodometric titration [9] and found to be 3.02. Heat capacity was measured by ac calorimetry on an experimental setup and by the method described in [10]. Resistivity was measured by the standard four-probe method.

The temperature dependences of heat capacity measured for $Sm_{0.55}Sr_{0.45}MnO_3$ in the fields $H = 0$ and 26 kOe over the temperature range 100–180 K in the heating and cooling regimes are presented in Fig. 1. Field measurements were carried out after cooling the sample down to liquid nitrogen temperature in zero field. One can see in Fig. 1 that the heat capacity of $Sm_{0.55}Sr_{0.45}MnO_3$ exhibits hysteretic anomalies in the vicinity of T_c both with the field and without it. Measurements of magnetic susceptibility and thermal expansion of $Sm_{0.55}Sr_{0.45}MnO_3$ suggest that this compound undergoes magnetic and structural phase transitions in the vicinity of T_c. It is also seen from Fig. 1 that T_c depends on both the magnetic field H and the direction of temperature variation. In the absence of the field ($H = 0$), $T_c^+(0) = 128.6$ K for the heating regime (+) and $T_c^-(0) = 113.3$ K for the cooling regime (–). For $H = 26$ kOe, $T_c^+(26\text{ kOe}) = 152.7$ K and $T_c^-(26\text{ kOe}) = 150.6$ K. Therefore, T_c increases, while the hysteresis width decreases as the field grows: $\Delta T_c(0) = T_c^+(0) - T_c^-(0) = 15.0$ K for $H = 0$ and $\Delta T_c(26\text{ kOe}) = 2.0$ K for $H = 26$ kOe. The heat capacity jumps corresponding to critical temperatures were calculated by approximating the experimental data before and after the transition to give $\Delta C_p^+(0) = 4.3$ J/(mol K), $\Delta C_p^-(0) = 4$ J/(mol K), and $\Delta C_p^+(26\text{ kOe}) = \Delta C_p^-(26\text{ kOe}) = 8.7$ J/(mol K). Considering that the hysteresis in magnets may be observed because of slow relaxation, measurements were carried out with different rates of temperature variation and different thermocycling intervals. It was found that the T_c values and, hence, ΔT_c did not change either with the field or without it. The points on the heat capacity curves for $Sm_{0.55}Sr_{0.45}MnO_3$ before and after the transition do not match the curve approximated by a single Debye interpolation formula, as happens for manganates of other compositions [11, 12]. Instead, the lattice heat capacity changes continuously near T_c.

The temperature dependences of resistivity measured in the cooling and heating regimes in fields 0, 13, and 26 kOe are shown in Fig. 2. One can see that the resistivity of $Sm_{0.55}Sr_{0.45}MnO_3$ also exhibits hysteresis, which, as in the case of heat capacity, is suppressed and shifts to higher temperatures in high fields. Such behavior of the resistivity of $Sm_{0.55}Sr_{0.45}MnO_3$ is qualitatively different from that of $La_{0.83}Sr_{0.17}MnO_3$, in which the temperatures of magnetic and structural phase transitions are also close [13].

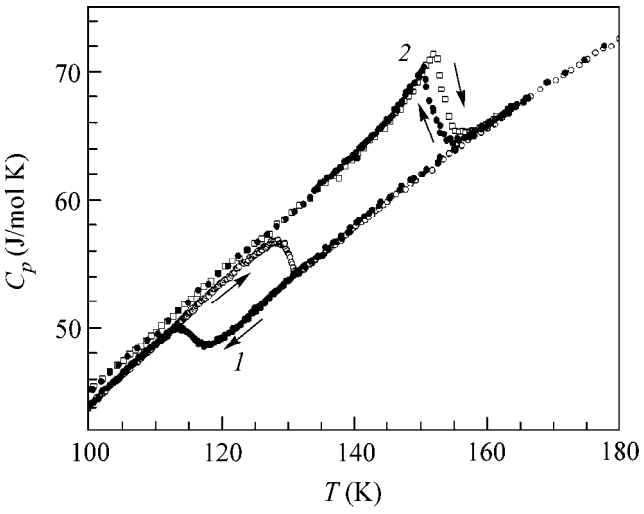

Fig. 1. Temperature dependence of the heat capacity of $Sm_{0.55}Sr_{0.45}MnO_3$: H = (*1*) 0 and (*2*) 26 kOe. Arrows indicate the direction of temperature change.

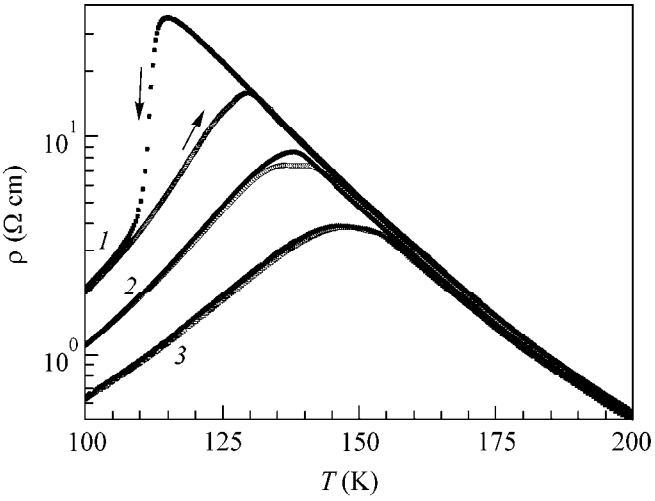

Fig. 2. Temperature dependence of the resistivity of $Sm_{0.55}Sr_{0.45}MnO_3$: H = (*1*) 0, (*2*) 13, and (*3*) 26 kOe. Arrows indicate the direction of temperature change.

These results can be rationalized in terms of the electron phase separation model. At $T < T_c$, $Sm_{0.55}Sr_{0.45}MnO_3$ can be imagined as an AFD matrix with inclusions of FM clusters in which the charge carriers are confined [1]. The FM clusters start to decompose near T_c. The charge carriers get free of the clusters, where they were confined at $T < T_c$, leading to a sharp decrease in resistivity at $T > T_c$. As the magnetic field increases, the FM clusters increase in size and their magnetic moments are aligned with the field. As a result, the kinetic energy of electrons in the clusters increases, making tunneling of charge carriers through the AFD barriers between the clusters easier and,

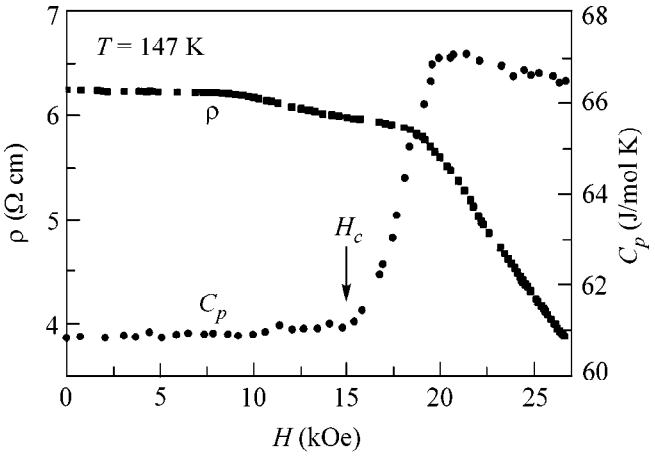

Fig. 3. Field dependence of the heat capacity and resistivity of $Sm_{0.55}Sr_{0.45}MnO_3$.

hence, reducing the resistivity. Moreover, the increase in magnetization in the bulk of FM clusters, together with the giant magnetostriction [7], give rise to the magnetocaloric effect, which manifests itself in the field-induced rise in heat capacity (Fig. 1). Near T_c, the second-order ferromagnet $\longrightarrow$ paramagnet phase transition induces simultaneous structural transition with changing lattice parameters [7]. The change in interatomic distances changes the energy of indirect exchange interaction between the Mn ions and, hence, changes the T_c value. Now, the reverse transition from the paramagnetic to the ferromagnetic phase occurs in the crystal structure at a different (according to our data, lower) T_c temperature, leading to the hysteretic behavior of the properties studied in this work for $Sm_{0.55}Sr_{0.45}MnO_3$. The field-induced rise in T_c and narrowing of ΔT_c are explained by the fact that, in parallel with the field-induced increase in T_c, as in usual ferromagnets, the pre- and posttransition lattice parameters in $Sm_{0.55}Sr_{0.45}MnO_3$ approach each other due to giant magnetostriction [7], resulting, according to the aforesaid, in the approach of T_c^+ and T_c^- and, hence, in the narrowing of ΔT_c. These arguments are supported by the measurements of the field-dependence isotherms for C_p and ρ at $T = 147$ K, as shown in Fig. 3. At $H = 0$, $Sm_{0.55}Sr_{0.45}MnO_3$ is in the paramagnetic state. As the field reaches its critical value $H_c = 15$ kOe, the FM clusters start to form and grow. As the clusters come into contact with each other, the resistivity sharply increases; i.e., the CMR effect occurs. One can see from Fig. 3 that the magnetic phase transition and the induced structural and metal–insulator transitions occur simultaneously and continuously.

According to the well-known Ehrenfest classification of phase transitions, the finite heat capacity jump and the continuous change in the properties of $Sm_{0.55}Sr_{0.45}MnO_3$ in the vicinity of T_c and H_c [14] are typical of second-order phase transitions, which are characterized by a finite transition width due to thermodynamic fluctuations. Therefore, our findings give evidence that the structural transition in $Sm_{0.55}Sr_{0.45}MnO_3$ is a second-order phase transition. The presence of hysteresis, although typical of first-order phase transitions, does not argue against this conclusion, because it is not a hysteresis in the ordinary sense but is a shift of critical temperatures.

Our speculations also confirm the results of measurements on single-crystal samples [8, 15]. The phase transitions with continuous change in the field dependence of magnetostriction and the temperature dependence of lattice parameters were observed, respectively, for $Sm_{0.55}Sr_{0.45}MnO_3$ and compositionally close $(Nd_{0.06}Sm_{0.94})_{0.5}Sr_{0.5}MnO_3$. However, the authors of [8] explained the anomalies in these samples by a field-induced first-order phase transition accompanied by giant magnetostriction and, in a more recent work [15], probably to moderate this categorical assertion, by a phase transition reminiscent of a first-order phase transition with the reduction of the Sm amount in the formula unit. As for the increase in the transition width because of the grain-size effect in ceramics [16], a comparison with the data in [8, 15] shows that, in the ceramics studied in this work, the transition width is almost twice as narrow as in single crystals of the corresponding composition. This also gives support to the microanalytic data about the high quality of the $Sm_{0.55}Sr_{0.45}MnO_3$ ceramics, viz., low porosity, tight grain sintering, and single-phase composition.

This work was supported by the Russian Foundation for Basic Research (project no. 00-07-90241) and the INTAS (grant no. 97- 11954).

REFERENCES

1. É. L. Nagaev, Usp. Fiz. Nauk **166**, 833 (1996) [Phys. Usp. **39**, 781 (1996)].
2. Y. Tokura and Y. Tomioka, J. Magn. Magn. Mater. **200**, 1 (1999).
3. N. N. Loshkareva, Yu. P. Sukhorukov, S. V. Naumov, *et al.*, Pis'ma Zh. Éksp. Teor. Fiz. **68**, 89 (1998) [JETP Lett. **68**, 97 (1998)].
4. A. I. Abramovich, R. V. Demin, L. I. Koroleva, *et al.*, Pis'ma Zh. Éksp. Teor. Fiz. **69**, 375 (1999) [JETP Lett. **69**, 404 (1999)].
5. I. F. Voloshin, A. V. Kalinov, S. E. Savel'ev, *et al.*, Pis'ma Zh. Éksp. Teor. Fiz. **71**, 157 (2000) [JETP Lett. **71**, 106 (2000)].
6. C. Martin, A. Maignan, M. Hervieu, and B. Raveau, Phys. Rev. B **60**, 12191 (1999).
7. A. I. Abramovich, L. I. Koroleva, A. V. Michurin, *et al.*, Fiz. Tverd. Tela (St. Petersburg) **42**, 1451 (2000) [Phys. Solid State **42**, 1494 (2000)].
8. Y. Tomioka, H. Kuwahara, A. Asamitsu, *et al.*, Appl. Phys. Lett. **70**, 3609 (1997).

9. A. A. Bosak, O. Yu. Gorbenko, A. R. Kaul, *et al.*, J. Magn. Magn. Mater. **211**, 61 (2000).
10. Sh. B. Abdulvagidov, G. M. Shakhshaev, and I. K. Kamilov, Prib. Tekh. Éksp., No. 5, 134 (1996).
11. L. Ghivelder, I. Abrego Castillo, N. McN. Alford, *et al.*, J. Magn. Magn. Mater. **189**, 274 (1998).
12. M. N. Khlopkin, G. Kh. Panova, A. A. Shikov, *et al.*, Fiz. Tverd. Tela (St. Petersburg) **42**, 111 (2000) [Phys. Solid State **42**, 114 (2000)].
13. A. Asamitsu, Y. Moritomo, Y. Tomioka, *et al.*, Nature **373**, 407 (1995).
14. L. D. Landau and E. M. Lifshitz, *Statistical Physics* (Nauka, Moscow, 1976; Pergamon, Oxford, 1980), Part 1.
15. H. Kuwahara, Y. Moritomo, Y. Tomioka, *et al.*, Phys. Rev. B **56**, 9386 (1997).
16. P. Levy, F. Parisi, G. Polla, *et al.*, cond-mat/0005247 (2000).

Translated by V. Sakun

JETP Letters, Vol. 72, No. 9, 2000, pp. 468–471. Translated from Pis'ma v Zhurnal Éksperimental'noĭ i Teoreticheskoĭ Fiziki, Vol. 72, No. 9, 2000, pp. 673–678.

On the Role of Nonpolar Optical Scattering for a Delocalized Positronium in Ionic Crystals

I. V. Bondarev

Research Institute of Nuclear Problems, Belarussian State University, Minsk, 220050 Belarus

e-mail: bond@inp.minsk.by

Received October 5, 2000

The role of optical deformation-potential scattering is studied for the delocalized positronium atoms in ionic crystals. At high temperatures, when the scattering becomes substantial, it (unless forbidden by the selection rules) renormalizes the positronium–acoustic phonon coupling constant. Such a renormalization was experimentally justified by measuring the momentum distribution for a delocalized positronium in the MgF_2 crystal. A similar effect is predicted for a positronium in crystalline quartz at temperatures above the transition from α- to β-quartz (846 K). © *2000 MAIK "Nauka/Interperiodica".*

PACS numbers: 71.38.+i; 71.60.+z; 36.10.Dr

At present, the formation of a positronium (Ps), i.e., a bound system of an electron and a positron, has been experimentally established for the majority of crystalline dielectrics [1]. At reduced temperatures (below several tens of Kelvins), the Ps atom in well-purified ionic crystals and α-quartz (α-SiO_2) is delocalized and exists in a Bloch-like state. The formation of a Bloch-like positronium was experimentally confirmed by the observation of narrow peaks (central peak and satellite peaks spaced at a distance inversely proportional to the lattice parameter) in the momentum distribution of 2γ-decay photons emitted upon irradiation of crystals by low-energy positrons. As the temperature increases, the satellites in the momentum distribution of decay photons disappear, while the central peak drastically broadens, evidencing Ps self-trapping [2]. This effect of thermally activated positronium self-trapping was observed in many ionic crystals and theoretically analyzed in [3, 4]. Recent experiments showed that the sole exception is provided by MgF_2 and α-SiO_2 crystals [5]. In these crystals, Ps remains delocalized up to temperatures $T \sim 700$ K (this fact was theoretically explained in [4]). A drastic (anomalous) broadening observed for the central and satellite positronium peaks in MgF_2 at temperatures above 200 K failed to be explained by Ps acoustical deformation-potential (longitudinal acoustic phonons) scattering. This effect appears to indicate that an additional scattering mechanism is activated above 200 K and renormalizes the coupling constant to acoustical modes in such a way that it increases more than twofold in a narrow temperature interval from 200 to 355 K. An analogous effect was not observed for α-SiO_2, where the temperature broadening of the central and satellite positronium peaks in the temperature range 80–700 K was successfully explained by Ps scattering from the long-wavelength longitudinal acoustic phonons.

In the temperature Green's function formalism (see, e.g., [6]), the equilibrium momentum distribution of a Ps atom interacting with phonons can be written as [5]

$$N(p) \sim \int_0^\infty d\omega e^{-\omega/k_BT} \frac{\Gamma(p, \omega)}{(\omega - p^2/2M^*)^2 + \Gamma^2(p, \omega)}. \quad (1)$$

Here, the exponential factor indicates the Boltzmann statistics, because only one Ps atom is present in a sample under real experimental conditions. The remainder is the explicit form of the quasiparticle spectral distribution function, where $\Gamma(p, \omega)$ is the imaginary part of the mass operator of a positronium interacting with phonons [6]. In the weak Ps–phonon coupling limit (delocalized Ps), only the leading (second) order in interaction with phonons is ordinarily taken into account for this operator:

$$\Gamma(p, \omega) = \pi \sum_{\mathbf{q}} |V_{\mathbf{q}}|^2 [(n_{\mathbf{q}} + 1)\delta(\omega - E_{\mathbf{k}+\mathbf{q}} - \hbar\omega_{\mathbf{q}}) + n_{\mathbf{q}}\delta(\omega - E_{\mathbf{k}+\mathbf{q}} + \hbar\omega_{\mathbf{q}})], \quad (2)$$

where $V_{\mathbf{q}}$ is the matrix element of interaction, $E_{\mathbf{k}} = \hbar^2\mathbf{k}^2/2M^*$ is the energy of a Ps with band mass M^* and quasi-momentum $\mathbf{k} = \mathbf{p}/\hbar$, $n_{\mathbf{q}} = \{\exp(\hbar\omega_{\mathbf{q}}/k_BT) - 1\}^{-1}$ is the phonon distribution function, and $\omega_{\mathbf{q}}$ is the frequency of a phonon with wavevector $\mathbf{q}$. With allowance

made only for the acoustical deformation-potential scattering, Eq. (2) transforms to [5]

$$\Gamma(p, \omega) \equiv \Gamma^{(a)}(p, \omega) = \frac{E_d^2 k_B T M^{*3/2}}{\sqrt{2}\pi\hbar^3 u^2 \rho}\sqrt{\omega}, \qquad (3)$$

where E_d is the constant of Ps coupling to the deformation potential of acoustical modes and u and ρ are the velocity of longitudinal acoustic phonons and the crystal density, respectively.

Equations (1) and (3) adequately describe the temperature broadening of the Ps momentum distribution in the temperature range 80–700 K for α-quartz but do not explain it for MgF_2 at temperatures above 200 K. In the latter case, the corresponding broadening is stronger and can only be explained if one postulates that the E_d constant increases with temperature (renormalizes) in the range 200–355 K from 7.6 eV below 200 K to 16 eV above 355 K [5].

In this work, the role of scattering by nonpolar optical modes is analyzed for a delocalized Ps atom in ionic crystals. The interaction of a Ps with the polarization field generated by lattice displacements is ignored for both acoustical and optical modes because of the electroneutrality of the Ps [7]. It is shown that, at temperatures where the scattering by nonpolar optical modes becomes significant (unless forbidden by the selection rules), it renormalizes the coupling constant to acoustical modes, thereby explaining the anomalous broadening of the Ps momentum distribution in MgF_2 observed in [5]. An analogous effect is predicted for a Ps in crystalline quartz above the temperatures of transition from α- to β-quartz at 846 K.

Scattering by optical modes and its role for a delocalized Ps in ionic crystals. It is known that scattering by the long-wavelength nonpolar optical modes (i.e., by the short-range deformation potential of optical modes) may play a significant part in crystals with two or more atoms in the unit cell [8–10]. As distinct from the long-wavelength acoustic modes, for which the interaction energy is proportional to the difference in lattice displacements of the neighboring atoms, the optical lattice displacements directly influence the energy of a particle in the band. In crystals where thermally activated Ps self-trapping does not occur, e.g., in MgF_2 and α-SiO_2, the scattering by optical modes may become significant for the delocalized Ps at elevated temperatures, when a sufficient number of optical phonons are excited and the corresponding coupling constant (optical deformation potential constant) is nonzero, according to the selection rules dictated by the local symmetry of a given point in the Brillouin zone [9, 10]. Indeed, although the acoustic phonons are much greater in number than the optical phonons, the square of the matrix element of the interaction with the acoustic phonons is smaller by a factor of $1/qa$ ($\gg 1$) (q is the modulus of phonon wavevector and a is the lattice parameter) [8]. For this reason, the scattering by nonpolar optical modes may become appreciable even at not too high temperatures (> ~100 K).

The Hamiltonian for the positronium interaction with nonpolar optical phonons (deformation potential of optical modes) can be written as [10]

$$H_{\text{int}}^{(o)} = \sqrt{\frac{\bar{M}}{M}}\mathbf{D}_o \times \mathbf{u}_o \simeq \sum_{\mathbf{k},\mathbf{q}} V_{\mathbf{q}}^{(o)} a_{\mathbf{k}+\mathbf{q}}^{+} a_{\mathbf{k}} (b_{\mathbf{q}o} - b_{-\mathbf{q}o}^{+}), \qquad (4)$$

where $\mathbf{D}_o$ is the vectorial optical deformation potential constant; $\mathbf{u}_o$ is the optical lattice displacement; and $\bar{M}$ and M are the reduced mass of the pair and the total mass of all atoms in the unit cell, respectively. The right-hand side of Eq. (4) is the secondary quantized interaction Hamiltonian written in the isotropic approximation without regard for the umklapp processes and the contribution from the Ps atomic form factor (see, e.g., [11]). In Eq. (4), $a_{\mathbf{k}}^{+}(a_{\mathbf{k}})$ and $b_{\mathbf{q}o}^{+}(b_{\mathbf{q}o})$ are the operators of creation and annihilation of, respectively, the Ps atom with quasi-momentum $\mathbf{k}$ and the long-wavelength optical phonon with the constant frequency ω_o and the wavevector $\mathbf{q}$:

$$V_{\mathbf{q}}^{(o)} = -iD_o\sqrt{\frac{\hbar}{2MN\omega_o}}, \qquad (5)$$

where $D_o = |\mathbf{D}_o|$ and N is the number of unit cells in a crystal.

Substituting matrix element (5) into Eq. (2) and carrying out simple mathematics, one obtains for the contribution from the nonpolar optical scattering to the imaginary part of the Ps mass operator

$$\Gamma^{(o)}(p, \omega) = \frac{D_o^2 M^{*3/2}\sqrt{\omega}}{2\sqrt{2}\pi\hbar^2\rho\omega_0}\left[(n(\omega_o)+1)\theta\left(1-\frac{\hbar\omega_o}{\omega}\right)\times\sqrt{1-\frac{\hbar\omega_o}{\omega}} + n(\omega_o)\sqrt{1+\frac{\hbar\omega_o}{\omega}}\right], \qquad (6)$$

where $n(\omega_o) = \{\exp(\hbar\omega_o/k_BT) - 1\}^{-1}$ is the Bose–Einstein distribution function for optical phonons and $\theta(x)$ is the Heaviside unit step function. The total expression (allowing for the scattering by acoustical and optical modes) for the imaginary part of the positronium mass operator is obtained by the summation of Eqs. (3) and (6):

$$\Gamma(p, \omega) = \Gamma^{(a)}(p, \omega) + \Gamma^{(o)}(p, \omega) = \frac{\tilde{E}_d^2(\omega) M^{*3/2} k_B T}{\sqrt{2}\pi\hbar^3 u^2 \rho}\sqrt{\omega}, \qquad (7)$$

where

$$\tilde{E}_d(\omega) = \left\{ E_d^2 + \frac{\hbar u^2 D_o^2}{2k_B T \omega_o} \left[(n(\omega_o) + 1)\theta\left(1 - \frac{\hbar\omega_o}{\omega}\right) \times \sqrt{1 - \frac{\hbar\omega_o}{\omega}} + n(\omega_o)\sqrt{1 + \frac{\hbar\omega_o}{\omega}} \right] \right\}^{1/2} \quad (8)$$

is the effective positronium–phonon coupling constant. Equations (1), (7), and (8) describe the temperature dependence of the momentum distribution for a delocalized Ps scattered by acoustic and optical phonons. Taking into account that the main contribution to the integral in Eq. (1) comes from the region $\omega \sim k_B T$, the $\tilde{E}_d(\omega)$ function in Eq. (8) can be approximated by $\tilde{E}_d(T)$, whereupon the effective constant takes the form

$$\tilde{E}_d(T) \approx \left\{ E_d^2 + \frac{\hbar u^2 D_o^2}{2k_B T \omega_o} \left[(n(\omega_o) + 1)\theta\left(1 - \frac{\hbar\omega_o}{k_B T}\right) \times \sqrt{1 - \frac{\hbar\omega_o}{k_B T}} + n(\omega_o)\sqrt{1 + \frac{\hbar\omega_o}{k_B T}} \right] \right\}^{1/2}. \quad (9)$$

One can readily verify that at low temperatures $T \ll \hbar\omega_o/k_B$, when the optical phonons are not excited, Eq. (9) tends to the acoustical constant E_d. In the opposite limit $T \gg \hbar\omega_o/k_B$, the effective positronium–phonon coupling constant $\tilde{E}_d = \sqrt{E_d^2 + (uD_o/\omega_o)^2}$ is independent of temperature. Therefore, the nonpolar optical scattering renormalizes the Ps coupling constant to acoustic phonons at high temperatures. As was already pointed out, this is precisely what was observed for a delocalized Ps in the MgF_2 crystal. Hence, this effect can be explained by the nonpolar optical scattering of positronium. This conclusion is confirmed by a reasonable agreement between the experiment and the estimates made for the optical deformation potential constant D_o. Substituting the experimentally measured values of 7.6 eV (below 200 K) and 16 eV (above 355 K) [5], respectively, for E_d and $\tilde{E}_d$ in the high-temperature limit of Eq. (9), one arrives at the estimate $D_o/\omega_o \sim 2 \times 10^{-5}$ eV s cm^{-1} for Ps in MgF_2 (the estimates were made with $u \approx 7 \times 10^5$ cm/s obtained by averaging the sound velocity over different crystallographic directions [12]). Assuming that ω_o is equal to $\sim 5 \times 10^{13}$ s^{-1}, i.e., to the average frequency of acoustic phonons with wavevectors corresponding to the boundary of the Brillouin zone of the MgF_2 crystal {estimated from the relation $\omega_o \sim u\pi/(2a/3 + c/3)$, where $a = 4.64$ Å and $c = 3.06$ Å are the lattice parameters of MgF_2 [13]}, one obtains a reasonable value of $D_o \sim 1 \times 10^9$ eV/cm for the optical deformation-potential constant of the Ps atom in MgF_2. Note, for comparison, that the typical values of the corresponding constants for electrons and holes in semiconductors are $\sim 5 \times 10^8$ eV/cm [10]. In particular, $D_o = 7 \times 10^8$ eV/cm for electrons in germanium [14].

That nonpolar optical scattering of positronium occurs in the MgF_2 crystal and not in the α-SiO_2 crystal can be explained by the fact that the D_o constant becomes zero at the center (Γ valley) of the Brillouin zone of α-SiO_2, because the selection rules dictated by the local symmetry of the reciprocal lattice are not fulfilled at this point of the **k** space. For example, it is known that the zero-order scattering by optical phonons in a cubic lattice is allowed (forbidden) for the degenerate (nondegenerate) Γ valleys [9, 10]. This can readily be understood from the general group-theoretic considerations. The D_o constant is determined by the perturbation operator (in our case, the deformation potential of optical lattice modes) matrix element between the near-band-bottom Bloch-like states of a particle [8, 9]. For the nondegenerate Γ valleys of cubic crystals, this matrix element belongs to the identity representation of the crystal point group, whereas the optical phonon branches are threefold degenerate; i.e., the corresponding normal lattice modes belong to one of the three-dimensional representations. In such a situation, interaction (4) is not invariant under the action of the point group operations and, thus, is identically zero (in other words, $D_o \equiv 0$). For this reason, the scattering by optical phonons is absent in the nondegenerate and occurs in the threefold degenerate Γ valleys of cubic crystals. However, if the point group symmetry in the crystal is lower than cubic (noncubic crystals), then the three-dimensional representation of optical vibrations in the Γ valley is reducible. If, among the irreducible representations contained in the latter, there is a representation of dimensionality equal to the degeneracy multiplicity of the Γ valley, then the optical modes belonging to this representation will appear in interaction (4), making it invariant about the point group operations in the crystal. For these optical modes, $D_o \neq 0$ and the particle will experience nonpolar optical scattering.

The aforesaid allows the new interesting effect to be predicted for a delocalized Ps in crystalline quartz. As is known, crystalline quartz undergoes a phase transition from α to β phase at temperature above 846 K [15]. This is accompanied by increasing lattice symmetry from D_3 to D_6. The point group D_6 is isomorphic with the C_{6v} group of crystals with the wurtzite structure. Consequently, it has the same representations for the Γ valley of the Brillouin zone and, accordingly, the same selection rules for scattering by optical phonons (a detailed symmetry group analysis of the deformation properties of crystals with the wurtzite structure is given in monograph [9]). According to [9], the point group C_{6v} (and the isomorphic group D_6) allows the nondegenerate and the doubly degenerate Γ valleys in the Brillouin zone of the respective crystals, whereas

the allowable representations of optical phonon modes at the center of Brillouin zone are one- and two-dimensional. Because of this, whatever the degeneracy multiplicity of the Γ valley, there will always be an optical mode that belongs to the representation of dimensionality equal to this multiplicity. This mode will appear in interaction (4) and make a nonzero contribution to the particle scattering by optical modes in the Γ valleys of crystals with point groups C_{6v} and D_6. Hence it follows that the nonpolar optical scattering of Ps, although it is absent in the α-SiO_2 crystal, should occur after the transition of α-quartz to the β phase above 846 K and the anomalous broadening of momentum distribution, analogous to that observed in MgF_2, should be observed for Ps in the β-SiO_2 crystal.

I am grateful to L.V. Keldysh, L.I. Komarov, V.N. Kushnir, and I.D. Feranchuk for helpful discussions.

REFERENCES

1. A. Dupasquier, in *Positron Solid-State Physics*, Ed. by W. Brandt and A. Dupasquier (Amsterdam, North-Holland, 1983), p. 510.
2. J. Kasai, T. Hyodo, and K. Fujiwara, J. Phys. Soc. Jpn. **57**, 329 (1988).
3. I. V. Bondarev and T. Hyodo, Phys. Rev. B **57**, 11341 (1998).
4. I. V. Bondarev, Phys. Rev. B **58**, 12011 (1998).
5. Y. Nagai, M. Kakimoto, H. Ikari, and T. Hyodo, Mater. Sci. Forum **255–257**, 596 (1997).
6. G. D. Mahan, *Many-Particle Physics* (Plenum, New York, 1981).
7. O. V. Boev and K. P. Aref'ev, Izv. Vyssh. Uchebn. Zaved., Fiz. **25**, 118 (1982).
8. G. L. Bir and G. E. Pikus, Fiz. Tverd. Tela (Leningrad) **2**, 2287 (1960) [Sov. Phys. Solid State **2**, 2039 (1961)].
9. G. L. Bir and G. E. Pikus, *Symmetry and Deformation Effects in Semiconductors* (Nauka, Moscow, 1972; Wiley, New York, 1975).
10. B. K. Ridley, *Quantum Processes in Semiconductors* (Oxford, Clarendon Press, 1982; Mir, Moscow, 1986).
11. I. V. Bondarev, Pis'ma Zh. Éksp. Teor. Fiz. **69**, 215 (1999) [JETP Lett. **69**, 231 (1999)].
12. K. S. Aleksandrov, L. A. Shabanova, and V. I. Zinenko, Phys. Status Solidi **33**, K1 (1969).
13. *Chemist's Handbook*, Ed. by B. P. Nikol'skiĭ (Khimiya, Leningrad, 1971).
14. M. Neuberger, *Handbook of Electronic Materials* (Plemun, New York, 1971).
15. *Acoustical Crystals*, Ed. by M. P. Shaskol'skaya (Nauka, Moscow, 1982).

Translated by V. Sakun

JETP Letters, Vol. 72, No. 9, 2000, pp. 472–475. Translated from Pis'ma v Zhurnal Éksperimental'noĭ i Teoreticheskoĭ Fiziki, Vol. 72, No. 9, 2000, pp. 679–683.

Fine Structure and Inverse Population in the $MnK_{\beta 1}$ Spectra of $Mn_xZn_yFe_zO_4$ Ferrites

Z. A. Samoĭlenko, V. S. Abramov, and N. N. Ivakhnenko

Donetsk Physicotechnical Institute, National Academy of Sciences of Ukraine, Donetsk, 83114 Ukraine

Received October 6, 2000

The electronic structure of $Mn_xZn_yFe_zO_4$ single-crystal ferrites was investigated. The fine structure of their X-ray spectra was found to correlate with the populations of quantum states. A scheme is suggested for the evolution of the electronic structure with strengthening exchange interaction of valence electrons as the chemical composition of the system becomes more complex. The metal–insulator phase transition is possible in the range of compositions corresponding to densities from $\rho = 5.097$ g/cm^3 to $\rho = 5.125$ g/cm^3, where manganese changes its charge state. © *2000 MAIK "Nauka/Interperiodica".*

PACS numbers: 33.15.Pw; 33.20.Rm; 71.30.+h

Elucidation of the nature of charge and magnetic orderings and the electronic structures of high-T_c superconducting and magnetoresistive materials is a topical modern-day problem. The X-ray emission and absorption spectra have been very promising for these purposes [1]. Early studies of $Mn_xZn_yFe_zO_4$ ferrites have shown that even small variations in their chemical composition are accompanied by the distortion of long-range order in their crystal structure and by its clustering, leading to the nonlinear changes in magnetic parameters [2, 3]. Much as the variations in the interatomic interaction were examined in [4, 5], we studied the X-ray emission spectra of $MnK_{\beta 1}$, because the Mn ions play a leading part in the formation of atomic structure and in the magnetic ordering in our ferrites. To analyze these spectra, a "string model" was developed. This model correlates with the fine structure in the spectra and allows one to predict and reveal the inversion mechanism of repopulation (inversion) of the Mn electronic states in the course of changing chemical composition of ferrites Cm-5 ($0.50Fe_2O_3 + 0.298MnO + 0.202ZnO$), Cm-6 ($0.5343Fe_2O_3 + 0.2915MnO + 0.1742ZnO$), Cm-7 ($0.5897Fe_2O_3 + 0.2377MnO + 0.1706ZnO$), Cm-1 ($0.6014Fe_2O_3 + 0.1379MnO + 0.2607ZnO$), and Cm-3 ($0.4645Fe_2O_3 + 0.2974MnO + 0.2381ZnO$). The samples were recorded and are presented in Figs. 1 and 2 in the order of increasing X-ray density from $\rho = 5.030$ g/cm^3 to $\rho = 5.140$ g/cm^3.

The experimentally observed variations of the $MnK_{\beta 1}$-line fine structure (manifesting itself as a multitude of shapes for the samples studied, Fig. 1) were analyzed by decomposing the β_1 line in multiplets with rigidly fixed energies E_1, E_2, …, E_6. The energies were estimated theoretically and found to be (eV) $E_1 = 6493.76$, $E_2 = 6494.67$, $E_3 = 6495.05$, $E_4 = 6495.32$, $E_5 = 6496.83$, and $E_6 = 6497.90$. In the experimental spectra, the intensity ordinates corresponding to particular energy values E_1, E_2, …, E_6 were measured and normalized separately for each sample. The maximum values of the intensity were set equal to unity, and the remaining values were estimated according to the respective proportions. The resulting evolution of the $MnK_{\beta 1}$-line shape in the samples is presented in Fig. 2. It reflects the variation of energy level populations with a change in the chemical composition of the $Mn_xZn_yFe_zO_4$ ferrite.

At the same time, the stick spectra of the $I(E)$ intensities indicate that, on going from Cm-5 to Cm-3, the population predominance shifts from the E_3 and E_4 states (Cm-5) to the E_5 state (Cm-3). In the Cm-6, Cm-1, and Cm-7 samples, this transition is accompanied by a gradual decrease in the intensity of the low-energy E_1, E_2, E_3, E_4 group of states and the strengthening of the high-energy E_5, E_6 group. This experimental result proves the population redistribution (inversion) among the Mn K states and gives evidence for a possible metal–insulator phase transition.

According to our microscopic model, the β_1 line is a multiplet with energies E_1, E_2, … E_6. In this ("string") model, the dominant mode ${}_3Mn^0$–${}_dMn$–${}_3Mn^0$ and the soft vibrational modes of the complexes of the ${}_2O^-$–${}_4Mn^+$ type are responsible for the energetic position of the multiple β_1 line. The magnetic ${}_3Mn^0$ ions (electronic configuration $3d^64\bar{s}$, electronic spin $S = 3/2$, electronic orbital angular momentum $L = 2$, total electronic angular momentum $J = 7/2$, and nuclear spin $I = 5/2$) are in the $|F; m\rangle = |1; \pm 1\rangle$ quantum state and exchange-cou-

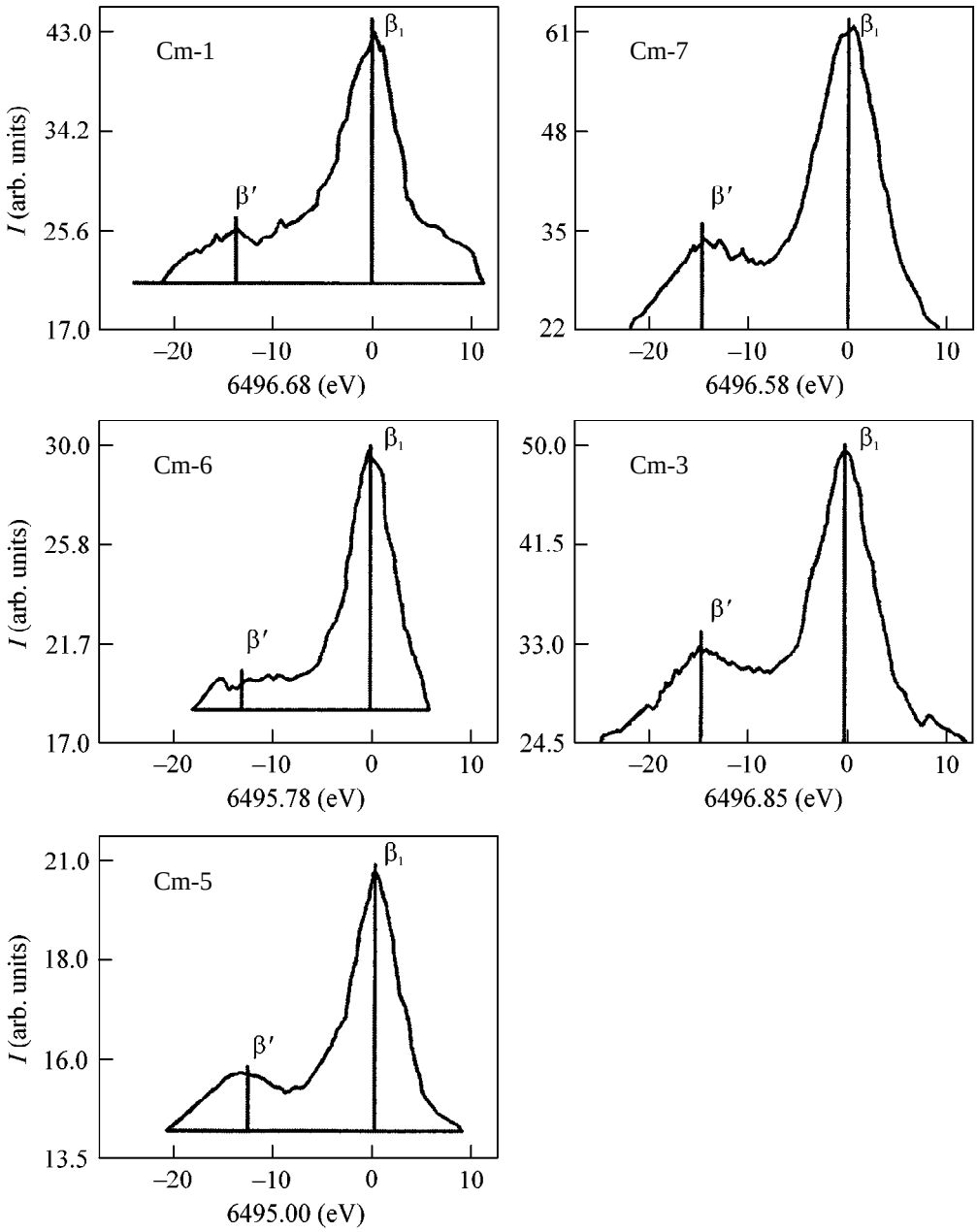

Fig. 1. X-ray $MnK_{\beta 1}$ spectra of the $Mn_xZn_yFe_zO_4$ samples (0 indicates the center of gravity of the line).

pled via the intermediate $_dMn$ ion (e.g., the diamagnetic $_4Mn^+$ ion with electronic configuration $3d^44s^2$, $S = L = 2$, and $J = 0$) to form a quasi-one-dimensional chain (string) with energy $E_0 = 6512.94$ eV of the dominant mode. The $_3Mn^0$ ions can be considered as composed of the $_1Mn^+$ ($3d^6$) core and an additional localized $4\bar{s}$ electron (the bar over s denotes that the spin of the $4\bar{s}$ electron is opposite to the total angular momentum of the $3d^6$ configuration). The nuclear spin of ^{55}Mn modifies the magnetic states of the $_3Mn^0$ ions in such a way that the total electronic angular momentum J is combined with the nuclear spin to form the total angular momentum F of the ion (in our case, $F = 1$). The crystallographic directions for the resulting valence bonds are specified by the parameter $m = 3\cos^2\theta - 1$, where θ is the angle between the z axis and the local symmetry axis (for our chain, $m = \pm 1$). The value $m = -1$ (i.e., $\cos^2\theta = 0$ and $\theta = 90°$) corresponds to the ($hk0$) plane.

The soft vibrational modes are described by the order parameter 2Δ. They are the normal modes of the chains formed by the $_2O^-$–$_4Mn^+$-type complexes (exchange-coupled via the intermediate $_dMn$ ions) in quantum states $|F; m\rangle = |5; \pm 0.5\rangle$, i.e., of the chains of

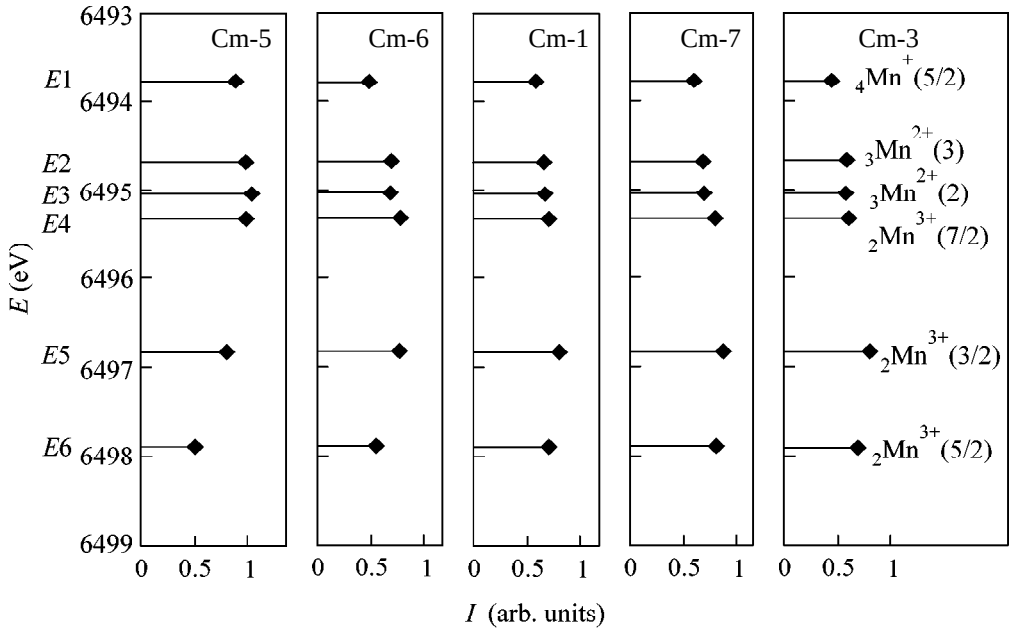

Fig. 2. Intensity distribution among the discrete energies of the $MnK_{\beta 1}$ multiplet.

the type $[_2O^{-}–_4Mn^{+}]–_dMn–[_2O^{-}–_4Mn^{+}]$. The total charge of this complex is zero. The intermediate $_dMn$ ions in the soft-mode chains correspond to the $_4Mn^{+}(5/2)$, $_3Mn^{2+}(3)$, $_3Mn^{2+}(2)$, $_2Mn^{3+}(7/2)$, $_2Mn^{3+}(3/2)$, and $_2Mn^{3+}(5/2)$ ions. The quantum states F of the intermediate ion are bracketed. The manganese ions are arranged in the order of their belonging to the discrete energies E_1, E_2, … E_6, which were calculated by formula $E_i = (E_0^2 - 4\Delta_i^2)^{1/2}$, where i = 1, 2, … 6. The ground electronic configurations and the valence and magnetic states of the manganese and oxygen ions and the complexes on their base are given in works [6, 7].

Condensation ($2\Delta_i \neq 0$) of the indicated soft modes and their coupling to the dominant mode are accompanied by the formation of quasi-two-dimensional structures with the required E_1, E_2, … E_6 energies. These structures are responsible for the fine structure of the β_1 line.

Let us analyze the experimental spectra in terms of the suggested model. One can see that the dominant-mode chain and the $_2O^{-}–_4Mn^{+}$ complexes in the soft-mode chains contain identical diamagnetic manganese ions. For this reason, the nonequivalence of interactions (fine structure) is caused solely by the presence of different intermediate manganese ions in the soft mode. The spectra in Fig. 2 indicate that the variations in the intensities of multiplets upon increasing the energy from E_1 to E_6 are caused by the contribution from the manganese ions that change their charge and quantum states in the order of increasing degree of ionization: from $_4Mn^{+}(5/2)$ to $_3Mn^{2+}(3)$ and further to $_2Mn^{3+}(5/2)$. In the Cm-5 and Cm-6 systems, the soft mode containing intermediate manganese ions $_4Mn^{+}(5/2)$, $_3Mn^{2+}(3)$, $_3Mn^{2+}(2)$, and $_2Mn^{3+}(7/2)$ dominates, respectively, the populations of the E_1, E_2, E_3, and E_4 levels, leading to the anisotropic increase in the intensities of the β_1 peak and to its sharpening in the spectrum of the Cm-6 sample (Fig. 1). The fact that the β' peak for the Cm-6 sample is smeared indicates that the electronic subsystem and the lattice are unstable, causing structural disorder typical of the critical state of concentration phase transition. In the remaining samples, the shape of β' is clearer. For the compositions of the Cm-1 and Cm-7 samples, the populations of the E_4 and E_5 levels due to the $_2Mn^{3+}(7/2)$ and $_2Mn^{3+}(3/2)$ ions are the greatest, leading to a change in the asymmetry of the β_1 peak and the appearance of a sharp maximum on the side corresponding to the E_4 and E_5 energies (Fig. 1). In addition, the β_1 profile in the spectrum of Cm-1 is structured and shows side peaks whose positions correspond to E_1 and E_6. This suggests that the populations of these levels are localized; i.e., the overlap is weak. At the same time, the extreme samples (Cm-5 and Cm-3) are characterized by a strong exchange interaction between the levels, as is evident from the smooth shape of the β_1 line (Fig. 1). It is found experimentally that, on going from Cm-5 to Cm-3, the center of gravity of the β_1 line shifts to high energies (Fig. 1). This correlates with the theoretically predicted positions of the dominant energy states in the E_1, E_2, … E_6 group and gives evidence for the strengthening of the degree of ionization of manganese in the above-mentioned order.

The facts reported in this paper demonstrate that the level populations in the $Mn_xZn_yFe_zO_4$ samples are gov-

erned by a particular type of the intermediate $_d$Mn ion and the corresponding potential "well" depth. For instance, the population distribution among the levels in the Cm-5 sample is virtually normal (equilibrium); i.e., the deeper (energetically lower) the well, the higher the population. However, beginning with the Cm-1 sample, the level populations are inverted; i.e, the shallower (energetically higher) wells are more populated, indicating the onset of a nonequilibrium metastable state.

Different intermediate ions occupy different crystallographic positions in the ferrite structure. The nonequivalence in the energy level populations induces local distortions in the crystal lattice and ensuing local mesoscopic-scale distortion of the long-range order in a solid solution, resulting in a clustered crystal structure and a weak ferromagnetism of the Dzyaloshinski–Moriya type.

REFERENCES

1. G. M. Eliashberg, in *Physical Properties of High-T_c Superconductors*, Ed. by D. M. Ginsberg (World Scientific, Singapore, 1989; Mir, Moscow, 1990).
2. V. I. Arkharov, Z. A. Samoĭlenko, V. V. Pashchenko, *et al.*, Neorg. Mater. **29**, 827 (1993).
3. V. V. Pashchenko, A. M. Nesterov, V. I. Arkharov, *et al.*, Dokl. Akad. Nauk SSSR **318**, 371 (1991).
4. A. T. Shuvaev, Izv. Akad. Nauk SSSR, Ser. Fiz. **25**, 986 (1991).
5. V. D. Okunev and Z. A. Samoĭlenko, Pis'ma Zh. Éksp. Teor. Fiz. **53**, 42 (1990) [JETP Lett. **53**, 44 (1991)].
6. V. S. Abramov, V. P. Pashenko, S. I. Khartsev, *et al.*, Funct. Mater. **6**, 64 (1999).
7. V. I. Abramov and A. I. Linnik, Fiz. Tekh. Vys. Davleniĭ **8**, 90 (1998).

Translated by V. Sakun

JETP Letters, Vol. 72, No. 9, 2000, pp. 476–479. Translated from Pis'ma v Zhurnal Éksperimental'noĭ i Teoreticheskoĭ Fiziki, Vol. 72, No. 9, 2000, pp. 684–688.

Observation of the Interaction between Landau Levels of Different Two-Dimensional Subbands in GaAs in a Normal Magnetic Field[1]

D. Yu. Ivanov[1], E. Takhtamirov[2], Yu. V. Dubrovskii[1], V. A. Volkov[2], L. Eaves[3], P. C. Main[3], M. Henini[3], D. K. Maude[4], J.-C. Portal[4,7], J. C. Maan[5], and G. Hill[6]

[1] *Institute of Microelectronic Technology and Ultrahigh-Purity Materials, Russian Academy of Sciences, Chernogolovka, Moscow region,142432 Russia*

e-mail: ivanovd@ipmt-hpm.ac.ru

[2] *Institute of Radio Engineering and Electronics, Russian Academy of Sciences, ul. Mokhovaya 18, Moscow, 103907 Russia*

[3] *The School of Physics and Astronomy, University of Nottingham, Nottingham NG7 2RD, United Kingdom*

[4] *Grenoble High Magnetic Field Laboratory, MPI-CNRS, BP166 38042 Grenoble Cedex 9, France*

[5] *High Field Magnet Laboratory, Research Institute for Materials, University of Nijmegen, 6525 ED Nijmegen, The Netherlands*

[6] *Department of Electrical Engineering, University of Sheffield, Sheffield S3 3JD, United Kingdom*

[7] *Institut Universitaire de France, Institut National des Sciences Appliquees, F31077 Toulouse Cedex 4, France*

Received September 26, 2000; in final form, October 11, 2000

Tunnel current measurements between strongly disordered two-dimensional electron systems in a perpendicular magnetic field are presented. Two-dimensional electron accumulation layers are formed by an extremely narrow layer of Si donors (Si delta doping) in GaAs on either side of an AlGaAs tunnel barrier. Strong interaction between Landau levels of the two-dimensional subbands in each accumulation layer is observed as an anticrossing of the related peak positions in the tunnel current vs. voltage curves as a function of magnetic field. The splitting of the interacting Landau levels is about 10 meV, which cannot be explained by nonparabolicity of the conduction band in GaAs. A possible reason for the observed interaction connected with the collective excitations in the 2DES is discussed. © *2000 MAIK "Nauka/Interperiodica".*

PACS numbers: 71.70.Di; 73.40.Gk; 71.55.Eq; 71.45.Gm; 73.20.Mf

In the case of a spherical energy-band model, there is no interaction between Landau levels of different two-dimensional subbands in a normal magnetic field and the intersection (crossing) of two Landau levels is allowed [1]. Interaction between Landau levels has been observed previously only in tunneling studies of surface quantization in narrow gap PbTe [2]. In this case, weak coupling can have a large effect, which leads to the anticrossing effect observed in tunneling spectra.

As far as we know, a similar effect has not been observed in wide band gap semiconductors, e.g., GaAs. This may be understood as follows: to observe interaction between Landau levels in tunneling experiments, it is necessary to detect both tunneling processes with Landau level index change and with Landau level index conservation. The former is usually weak in comparison with the latter, since it takes place only in the presence of strong elastic scattering in the tunnel structures. In relatively clean samples, which are mainly used for tunnel current measurements, the experimental features related to tunneling with or without conservation of Landau level index are quite different in amplitude, and even if they do cross, it is difficult to judge the nature of the interaction between Landau levels.

In this work, we investigate the current–voltage characteristics of the heterostructure GaAs/AlGaAs/GaAs with tunneling between strongly disordered two-dimensional electron systems (2DES) in a magnetic field parallel to the direction of current flow. Due to the strong elastic scattering-assisted tunneling, the amplitude of the peaks related to the tunneling between Landau levels is of the same order of magnitude for processes both with Landau level index conservation and without. This allows us to study the interaction between the Landau level ladders of the two 2DES. We find that the interaction between Landau levels of the different two-dimensional subbands in GaAs is very strong and the observed splitting is about 10 mV, comparable to the splitting observed in PbTe [2]. Possible reasons for the observed interaction are discussed.

[1] This article was submitted by the authors in English.

0021-3640/00/7209-0476$20.00 © 2000 MAIK "Nauka/Interperiodica"

The MBE-grown sample was a single barrier GaAs/$Al_{0.4}Ga_{0.6}As$/GaAs heterostructure with a 12-nm-thick barrier. The barrier was separated from the highly doped bulk contact regions by 50-nm-thick undoped GaAs spacer layers. To form the 2DES, we used Si donor sheets with a concentration of 3×10^{11} cm^{-2} located 5 nm from each side of the barrier. Samples were fabricated into mesas of diameter 100–400 μm. The tunneling transition probability of the main barrier is much lower than that of the spacer regions, so that almost all of the applied voltage is dropped across the barrier. Measurements of the Shubnikov–de Haas (SdH)-like oscillations in the tunnel current gave electron sheet concentrations approximately equal to the donor doping levels. The schematic band diagram of the structure at zero bias is shown in the insert of Fig. 1. The typical electron mobility in the 2DES is estimated to be about $\mu = 1000$ cm^2 V^{-1} s^{-1} at 4.2 K. In our experiments, electron transport along the layers does not contribute to the measured tunnel current, which flows perpendicular to the plane of the barrier.

Figure 2 shows the differential tunnel conductance G at 4.2 K, measured using standard lock-in techniques, versus external bias voltage V_b at various magnetic fields of up to 15 T. In zero magnetic field (lowest curve in Fig. 2), the differential conductance has a peak at zero bias and two pronounced shoulders at higher voltage for both polarities. We argue that the zero voltage peak reflects resonant tunneling between the ground states of the 2DESs and that the shoulders are due to resonant tunneling between the ground state of the emitter 2DES (ground 2D subband, $n = 0$) and first exited state (excited 2D subband, $n = 1$) in the collector 2DES. The observation of a pronounced maximum at zero bias in zero magnetic field indicates that, despite the relatively large number of scattering centers in the 2D layers, the conservation of in-plane momentum is important for the tunneling process. The evolving structure in the curves with increasing magnetic field is due to resonant tunneling between different Landau levels, which we now consider in more detail.

Around $B = 6$ T, which is close to Landau level filling factor $n = 2$ for the 2DES, the measured $G(V)$ curves show (see Fig. 2) a pronounced minimum at zero voltage. With a further increase in the magnetic field, the minimum of the differential conductance at zero bias gradually becomes a maximum. The details of the equilibrium tunneling processes around zero bias with magnetic field have been discussed previously [3].

In this work, we concentrate on the evolution of the structure related to tunneling between different Landau levels. We focus on the shoulders in G, which are indicated by circles in Fig. 2. Their fan diagram (positions on the voltage scale versus magnetic field) is shown in Fig. 3. For simplicity, we consider only negative bias; the observed structure is symmetrical around zero bias, except for certain details which we will not consider here. To understand the data, it is easiest to begin with

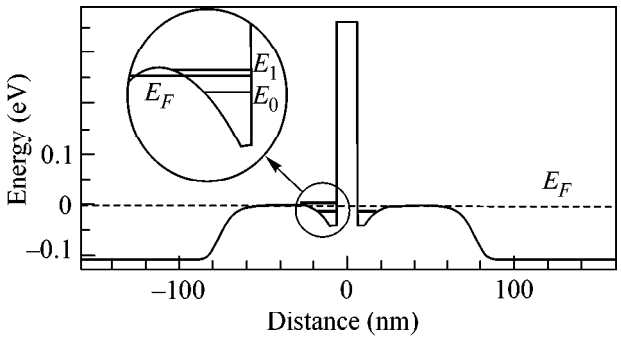

Fig. 1. A schematic band diagram of the structure at zero bias. Insert shows the energy levels in the two-dimensional system in more detail. E_0 and E_1 are, correspondingly, the energy of the ground and excited two-dimensional states. E_F is the Fermi energy.

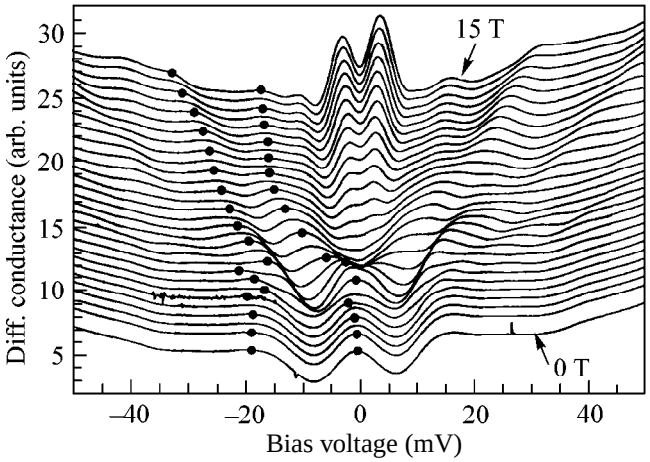

Fig. 2. Tunneling differential conductance at 4.2 K as a function of external voltage in different magnetic fields for a mesa of diameter 400 μm. The curves are shifted for clarity in the vertical direction. The lowest curve is for $B = 0$ T, and the top one for $B = 15$ T. Magnetic-field step between curves $\Delta B = 0.5$ T. The curve for $B = 0.5$ T is absent. Circles mark the peaks whose evolution with magnetic field are discussed in the paper.

the curves at high magnetic fields. At fields higher than 12 T, circles correspond to the tunneling between the 1st Landau level ($N = 0$) of the ground subband state in the emitter ($n = 0$), and the 2nd Landau level ($N = 1$) of the ground subband state in the collector ($n = 0$), without Landau level index conservation, i.e., ($n = 0$, $N = 0$) $\longrightarrow$ ($n = 0$, $N = 1$) tunneling. The dashed line labeled A has a slope equal to $L\hbar\omega_C$, where $\hbar\omega_C$ is the cyclotron energy and L is the electrostatic leverage factor, equal to 1.28 for our structure. This gives the positions of the peaks for $\Delta N = 1$ tunneling in the case of ideal Landau level quantization. The dashed line labeled B gives the positions of the peaks for ideal $\Delta N = 2$ tunneling. For broadened Landau levels, the differential tunneling conductance which we measure reflects the joint den-

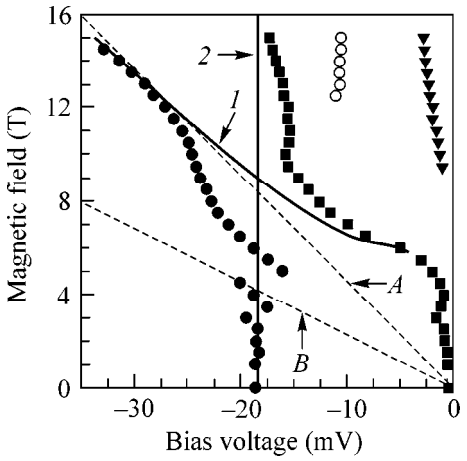

Fig. 3. Peak positions on the voltage scale as a function of magnetic field. Circles, squares, and triangles represent experimental data and are discussed in the text. Curve 1 is calculated peak positions for the ($n = 0$, $N = 0$) ⟶ ($n = 0$, $N = 1$) tunneling process, where n is the main quantum number of the two-dimensional state, N—Landau level index. Vertical line, labeled *2*, represents the expected position of the peak for the ($n = 0$, $N = 0$) ⟶ ($n = 1$, $N = 0$) tunneling process. Both curves *1* and *2* are calculated in the absence of the interaction between Landau levels. Lines *A* and *B* have slopes equal to $L\hbar\omega_C$ and $2L\hbar\omega_C$, respectively, where $\hbar\omega_C$ is the cyclotron energy and L is the leverage factor in the structure. These lines represent tunneling between Landau levels with $\Delta N = 1$ and $\Delta N = 2$, correspondingly, in the case of the ideal Landau level quantization.

sity of states at the Fermi levels of the emitter 2D electron system. In this case, the calculated position of the peaks for ($n = 0$, $N = 0$) ⟶ ($n = 0$, $N = 1$) tunneling is shown by the curve labeled *1*. The positions of the peaks related to $N = 0$ processes do not depend on magnetic field. Evidently, the peak position for ($n = 0$, $N = 0$) ⟶ ($n = 0$, $N = 1$) should correspond to the vertical line labeled *2*. This coincides with the position of the peak due to resonant tunneling between the ground 2D state in the emitter and the first excited state 2D state in the collector with $B = 0$. Without interaction between Landau levels, the lines describing peak positions of the different processes versus magnetic field dependences should intersect, as do curves *1* and *2*. In contrast, curves presented as circles and squares in Fig. 3 exhibit obvious anticrossing, which is a manifestation of the interaction between Landau levels ($n = 0$, $N = 1$) and ($n = 1$, $N = 0$) of the different subbands in the collector. The observed splitting is about 10 meV. Some deviations are also evident around the point where the line labeled *B* intersects vertical line *2*. These deviations indicate that interaction between Landau levels ($n = 0$, $N = 2$) and ($n = 1$, $N = 0$) in the collector 2DES also takes place, but the resolution of the features is not high enough. For completeness, we also indicated the position of the peaks around zero voltage (triangles in Fig. 3), which are due to the development of the tunneling gap at the Fermi level in a magnetic field [3]. The origin of the additional peaks, which appear in magnetic fields higher than 12 T around 14 mV (open circles in Fig. 3), is not clear. We tentatively propose that they are related to spin splitting in the 2DES.

We now discuss possible mechanisms for the strong (~10 meV) anticrossing of the Landau levels $N = 1$ from the ground subband $n = 0$ and $N = 0$ from the excited subband $n = 1$. Naturally, such a mechanism should mix longitudinal and transverse motion of electrons in the 2D layer. Experiments in tilted magnetic fields have shown that the accuracy of the magnetic field orientation (**B** || **J**) is high enough to rule out the possibility that the anticrossing is due to effects associated with an unwanted in-plane component of the magnetic field. A second possible origin of the anticrossing is a weak nonparabolicity of the electron spectrum in GaAs. A qualitatively similar anticrossing was observed in the 2D layer of a highly nonparabolic material, PbTe [2]. But in the latter case, the strong anticrossing was caused by the fact that the main axes of the constant energy ellipsoids of the conduction band minimum (L point of the Brillouin zone) are not along the direction of growth. This is not the case for GaAs, and the theoretical estimation of contribution of the nonparabolicity yields an anticrossing effect of only ~1 meV—too small a value to account for our observations.

An alternative explanation of the anticrossing is connected with the collective excitations. It is necessary to consider possible mechanisms of the energy relaxation of an electron which tunnels onto the excited level in a system with a totally discrete spectrum. It is known that, if the energy gap between this level and the Fermi level is a multiple of the LO phonon energy, the energy relaxation will be governed by resonant emission of LO phonons. This corresponds to the appearance of the phonon replicas on the tunnel spectra. Otherwise such relaxation is forbidden. Nevertheless, in all cases, the relaxation accompanied by emission of 2D magnetoplasmons having a gap equal to the cyclotron frequency (intrasubband magnetoplasmons) or intersubband gap (intersubband plasmons [4]) is energetically allowed. Note that conservation of the momentum in these processes is provided by strong electron–impurity scattering in our "dirty" system. The observed anticrossing occurs at a magnetic field which corresponds to the crossing of the intra- and intersubband magnetoplasmons. Accordingly, the observed anticrossing of two peaks may be interpreted as a manifestation of the relaxation on "hybrid" intra-intersubband magnetoplasmons. In the case of $B = 0$, such hybrid plasmons were theoretically investigated in [5, 6]. It could be expected that the anticrossing in this case would be of the order of the Coulomb interaction in the 2DES, which is just what has been found in measurements.

In summary, we have investigated tunneling processes between strongly disordered 2D electron systems in a quantized magnetic field parallel to the current. The manifestation of the strong interaction

between Landau levels of different two-dimensional subbands in GaAs has been observed experimentally. The explanation of the observed anticrossing related to the excitation of inter- and intrasubband magnetoplasmons in the 2DES is proposed.

This work was supported in part by the INTAS (grant no. 97-11475), the PICS-CNRS (grant no. 628, France), the Russian Foundation for Basic Research (project nos. 98-02-17642, 98-02-22008, and 99-02-17592), the Russian national programs "Physics of Solid-State Nanostructures" (grant nos. 97-1057, 99-1124), "Physics of Quantum and Wave Processes" (V.3), "Surface Atomic Structures" (3.1.99, 3.11.99), and by the EPSRC (UK).

REFERENCES

1. C. B. Duke, Phys. Rev. **159**, 632 (1967); D. J. Ben-Daniel and C. B. Duke, Phys. Rev. **160**, 679 (1967); C. B. Duke, Phys. Lett. A **24**, 461 (1967); G. A. Barraf and J. A. Appelbaum, Phys. Rev. B **5**, 475 (1972).
2. D. C. Tsui, G. Kaminsky, and P. H. Schmidt, Phys. Rev. B **9**, 3524 (1974).
3. Yu. N. Khanin, Yu. V. Dubrovskii, E. E. Vdovin, *et al.*, Physica E (Amsterdam) **67**, 3836 (1991).
4. D. A. Dahl and L. J. Sham, Phys. Rev. B **16**, 651 (1977).
5. R. Z. Vitlina and A. V. Chaplik, Zh. Éksp. Teor. Fiz. **81**, 1011 (1981) [Sov. Phys. JETP **54**, 536 (1981)].
6. J. K. Jain and S. Das Sarma, Phys. Rev. B **36**, 5949 (1987).